Materials Research Bulletin 169 (2024) 112498

Contents lists available at ScienceDirect

Materials Research Bulletin

journal homepage: www.elsevier.com/locate/matresbu

Research Papers

Effect of dopant on ion-dynamics of sodium ion-based flexible polyblend electrolyte for electrochemical device application

Vipin Cyriac [a,b], Ismayil [b,*], Y.N. Sudhakar [c], Kuldeep Mishra [d], Z.E. Rojudi [e], M.S. Murari [f], I.M. Noor [e,g]

[a] Department of Sciences, Manipal Academy of Higher Education, Manipal, Karnataka 576104, India
[b] Department of Physics, Manipal Institute of Technology, Manipal Academy of Higher Education, Manipal, Karnataka 576104, India
[c] Department of Chemistry, Manipal Institute of Technology, Manipal Academy of Higher Education, Manipal, Karnataka 576104, India
[d] Department of Physics, Jaypee University, Anoopshahr, Uttar Pradesh 203390, India
[e] Ionic Materials and Energy Devices Laboratory, Physics Department, Faculty of Science, Universiti Putra Malaysia, UPM Serdang, Selangor Darul Ehsan 43400, Malaysia
[f] DST-PURSE Program, Mangalore University, Mangalagangotri 574199, India
[g] Physics Division, Centre of Foundation Studies for Agricultural Science, Universiti Putra Malaysia, Serdang, Selangor Darul Ehsan 43400, Malaysia

ARTICLE INFO

Keywords:
A. amorphous materials
C. X-ray diffraction
C. impedance spectroscopy
D. dielectric properties
D. ionic conductivity

ABSTRACT

This work examines the impact of $NaNO_3$ salt on a NaAlg: PVA blend polymer, focusing on charge carrier properties, such as number density (n), mobility (μ), and diffusion coefficient (D). It is found that the addition of $NaNO_3$ increased the room temperature conductivity from $(6.12\pm0.15) \times 10^{-8}$ S cm^{-1} (PNN0, salt-free) to $(6.50 \pm0.03) \times 10^{-6}$ S cm^{-1} (PNN15, 15 wt.% $NaNO_3$), influenced by increasing n compared to μ. Temperature-dependent conductivity revealed a significant influence of both n and μ on electrolyte conductivity, and the ion dynamics were explored using various formalisms. XRD studies showed reduced crystallinity owing to the interaction of Na^+ and NO_3^- with -OH groups, as confirmed by IR spectroscopy. Scanning electron microscopy confirmed salt deposits at higher concentrations. However, sufficient mechanical strength was observed for the optimally conducting sample. Obtained results showed the potential applications of the sample in electrochemical devices.

1. Introduction

Since the discovery of polymer electrolytes (PEs) in 1973 [1], considerable attention has been paid to the development of new PEs. In recent years, the development of solid polymer electrolytes (SPEs) with high ionic conductivity ($\sigma > 10^{-4}$ S cm^{-1} at room temperature) has received a boost for its applications in batteries, fuel cells, supercapacitors, and sensors due to its advantages over their liquid counterparts, such as leak-free, high thermal stability, low flammability, flexibility, and overall cell weight reduction. However, the critical advantages of polymer electrolytes are related to their processing and cost. Polymer electrolytes can be synthesized at lower temperatures, making them highly suitable for air-stable conditions and compatible with roll-to-roll manufacturing techniques [2]. Moreover, the interfacial contact between the electrode and polymer electrolyte is better than that of the ceramic electrolyte, leading to an improvement in the overall ion conduction properties. Therefore, the use of polymer electrolytes (PEs) is a practical and promising approach for the development of all-solid-state batteries. This is because of their unique combination of benefits in terms of both processability and performance.

However, polymer electrolytes suffer many challenges before they can be used in commercial energy storage devices. Particularly at room temperature or lower, the conductivity of SPEs is still insufficient for real-world applications. In addition, dendrite formation between the electrodes through the electrolyte must be suppressed to achieve extremely safe commercial applications. Hence, polymer electrolyte membranes must be developed conscientiously to minimize the trade-offs between all parameters.

The majority of polymer electrolytes use synthetic polymers such as poly (ethylene oxide) (PEO) and poly (vinyl pyrrolidone) (PVdF), which are mainly derived from petroleum products and, in the long run, create environmental pollution problems [3]. However, natural polymers are

* Corresponding author.
E-mail address: ismayil.mit@manipal.edu (Ismayil).

https://doi.org/10.1016/j.materresbull.2023.112498
Received 8 June 2023; Received in revised form 7 August 2023; Accepted 22 August 2023
Available online 23 August 2023

advantageous over synthetic polymers because they are low-cost, non toxic, biodegradable, and biocompatible [4]. To achieve high ionic conductivity, the polymer needs to have many functional groups with electronegative atoms, such as *-OH*, *-C = O*, etc., to solvate salts and to assist the ion hopping motion through the polymer matrix. Several biopolymers such as starch, gelatin, cellulose and its derivatives, chitosan, gellan gum, and alginic acid have been extensively studied. Among these, alginic acid, commonly known as alginate, is of particular interest. Alginates exist naturally in marine brown algae as calcium, magnesium, and sodium salts, forming an integral part of their cell walls. Sodium alginate (NaAlg), an anionic polysaccharide, is particularly noteworthy. It comprises units of (1–4)-linked β-D-mannuronic acid (M) and α-L-gluronic acid (G). Sodium alginate is highly regarded because of its remarkable biocompatibility, lack of toxicity and immunogenicity, biodegradability, and ability to form gels when exposed to divalent cations, such as calcium ions. [5]. It has been widely investigated for biomedical applications such as drug carriers [6]. The use of sodium alginate in the polymer electrolyte is preferred due to the presence of $-COO$ and $-OH$ group that may help for ion coordination and transportation. Moreover, NaAlg has an excellent ability to accommodate extremely high salt concentrations as a dopant. For example, at remarkably high salt concentrations (> 50 wt.%), ionic conductivity of the order of 10^{-3} Scm^{-1} at room temperature has been reported [7,8]. However, the reported system is a "salt in polymer" matrix.

Blending methods have been employed as an alternative strategy to enhance the physicochemical properties of individual polymers by incorporating them into other polymers. This approach aims to improve the overall characteristics of the polymers through blending. The compatibility of polymer molecules, as controlled by intermolecular interactions, has been reported to affect the properties of blends [9]. Although biopolymers have demonstrated good biocompatibility, their mechanical properties are inferior to those of synthetic polymers [10]. For example, NaAlg shows some stiffness and brittleness.

Consequently, the mechanical properties of NaAlg can be enhanced by incorporating poly (vinyl alcohol) (PVA) into sodium alginate (NaAlg). PVA is well known for its high elasticity and biocompatibility, making it an ideal blend material to improve the mechanical characteristics of NaAlg [11]. Owing to its affordability and exceptional attributes, including chemical stability, hydrophilicity, strong abrasion resistance, and favorable mechanical properties such as elongation, tensile strength, and flexibility, poly (vinyl alcohol) (PVA) is extensively employed as a blending material [12].

Due to numerous $-OH$ groups in the PVA polymer backbone, polymer blending is facilitated with NaAlg, which leads to good compatibility between the polymer blend [13]. Hence, NaAlg was the main component and PVA was the second component of the blend in this study. Furthermore, NaAlg-PVA-based polymer electrolyte membranes based on lithium [14], sodium [15], and potassium [16] were examined for electrochemical device applications. As part of the effort to reduce the dependence on petrochemical-based polymer electrolytes, the current work systematically focuses on the development of a biopolymer based on NaAlg-PVA. The influence of microstructural modifications and variations in room-temperature and high-temperature ion transport parameters caused by the complexation of the $NaNO_3$ salt were studied. $NaNO_3$ salt was used in this study because it has low lattice energy of 756.25 kJ mol^{-1} and can be handled at ambient temperatures [17], and a few systems based on $NaNO_3$ salts have been used for energy storage applications [18–20]. Therefore, we aim for the use of NaAlg-PVA/-$NaNO_3$ as a potential electrolyte for energy storage devices.

2. Experimental

2.1. Chemicals used

Sodium alginate (NaAlg) and poly (vinyl alcohol) (PVA, Mw: 85,000 g mol^{-1}) were procured from S.D. Fine Chem Ltd., without any further purification, was used to prepare the polymer blend. Sodium nitrate ($NaNO_3$, Mw: 84.99 g mol^{-1}) was used as an ionic dopant and procured from Merck Life Science.

2.2. Preparation of solid polymer electrolytes (SPEs)

SPEs consisting of sodium alginate (NaAlg) and poly (vinyl alcohol) (PVA) as a blend component and sodium nitrate ($NaNO_3$) as an ionic supplier were prepared by solution casting technique with de-ionised water as a common solvent. The blend components were taken in NaAlg: PVA weight ratio of 60 wt.%:40 wt.%. The amount of $NaNO_3$ salt added (m_s) into the blend system in weight percent was determined using Eq. (1)

$$m_s(wt.\ \%) = \frac{w_s}{w_s + w_p} * 100\% \quad (1)$$

Here, w_s is the mass of the salt, and w_p is the mass of the blend polymer. The salt weight ratio was varied from 5 to 30 wt.%. Beyond this composition, the formation of the free-standing film was impossible. Table 1 presents the sample designations.

The blend polymer and dopant salt were magnetically stirred at 60 °C for 24 h until a homogenous viscous solution was obtained. It was then poured into a polyethylene petri dish to undergo slow evaporation at room temperature, after which the free standing films were peeled off. The films were subsequently dried in an oven and stored in a vacuum desiccator until further characterization.

2.3. Sample characterizations

2.3.1. Fourier transform infrared (FTIR) spectroscopy

The complexation between the salt and polymer matrix was studied by room temperature FTIR spectroscopy (SHIMADZU IRPrestige-21 ATR-FTIR) in the wavenumber range of 4000 cm^{-1} to 400 cm^{-1} in transmittance mode with a resolution of 4 cm^{-1}.

2.3.2. X-ray diffraction (XRD)

X-Ray diffraction studies were done using Rigaku Miniflex 600, 5th Gen, to understand the variation in crystallinity of the prepared solid polymer electrolytes in the angular range of 5° and 90° at a scan rate of 2°min^{-1} with Cu-Kα (λ = 1.54 Å) as a resource.

2.3.3. Electrochemical impedance spectroscopy (EIS)

Electrochemical impedance spectroscopy (EIS) was carried out at room temperature and elevated temperatures using a Hioki IM3570 Impedance Analyzer to evaluate the ionic conductivity variation with the dopant. EIS measurements were performed by clamping the sample between ion-blocking stainless-steel electrodes and applying a 10 mV ac signal across the sample with a frequency range between 100 Hz and 4.5 MHz from room temperature (25 °C) to 120 °C. Measurements were taken at each set temperature as soon as the equilibrium was reached. The impedance data were then transformed into a dielectric format to investigate electrolyte ion dynamics. The real part of the complex permittivity ϵ' and the imaginary part of the complex permittivity ϵ'' were

Table 1
Designation, sample composition of prepared SPEs.

Designation	NaAlg/PVA: $NaNO_3$ (wt.%:wt.%)	NaAlg/PVA.	$NaNO_3$ (g)
PNN0	100:0	2.0	0
PNN5	95:5	1.9	0.1
PNN10	90:10	1.8	0.2
PNN15	85:15	1.7	0.3
PNN20	80:20	1.6	0.4
PNN25	75:25	1.5	0.5
PNN30	70:30	1.4	0.6

deduced using the real part of the complex impedance Z_r and the imaginary part of the complex impedance Z_i data as follows:

$$\epsilon' = \frac{Z_i}{\omega C_0 \left(Z_r^2 + Z_i^2\right)} \tag{2}$$

$$\epsilon'' = \frac{Z_r}{\omega C_0 \left(Z_r^2 + Z_i^2\right)} \tag{3}$$

Here C_0 is the vacuum capacitance. ω is the angular frequency deduced from $2\pi f$. Further, the real and imaginary parts of complex modulus, M', and M'' respectively, were derived as

$$M' = \frac{\epsilon'}{\epsilon'^2 + \epsilon''^2} \tag{4}$$

$$M'' = \frac{\epsilon''}{\epsilon'^2 + \epsilon''^2} \tag{5}$$

Furthermore, the tangent loss was calculated using Eq. (6).

$$tan\delta = \frac{\epsilon''}{\epsilon'} \tag{6}$$

2.3.4. Field emission scanning electron microscope (FESEM)

Variations in surface morphology were investigated using field-emission scanning electron microscopy (FESEM). To reduce the charging effects on the sample, it was coated with a thin layer of gold using a Quorum Gold sputtering unit for approximately 5 min. Elemental mapping was performed to assess the distribution of the various elements in the polymer matrix.

2.3.5. Thermal studies

The thermal parameters and thermal stability were examined using two analytical techniques: Differential Scanning Calorimetry (DSC) with a SHIMADZU DSC-60 PLUS instrument and Thermogravimetric Analysis (TGA) with a Hitachi STA7200 TGA-DTA instrument. Samples weighing approximately 5–8 mg were placed in a platinum crucible and heated at a constant rate of 10 °C min^{-1}. DSC measurements were conducted from room temperature to 200 °C in a nitrogen (N_2) gas atmosphere with a flow rate of 40 mL min^{-1}. TGA analysis (TGA) was carried out from room temperature to 500 °C in a nitrogen (N_2) gas atmosphere at a flow rate of 20 mL min^{-1}.

2.3.6. Linear sweep voltammetry (LSV)

Linear sweep voltammetry (LSV) was performed to evaluate the electrochemical stability window (ESW) of the samples using CH600E potentiostat. The electrolyte films were sandwiched between stainless steel electrodes in a configuration of SS|SPE|SS, and the voltage was scanned from 0 to 4 V at a scan rate of 5 mV s^{-1}.

2.3.7. Transference number measurement (TNM)

Transference number measurements (TNM) were performed using a Keithley 2636 B sourcemeter. A direct current (DC) voltage of 100 mV was applied to a symmetric cell configuration, which included an electrolyte layer positioned between the stainless-steel blocking electrodes. The current was continuously monitored to determine the ion transference number.

2.3.8. Mechanical properties

A Dak System Inc. 7200 series universal testing machine with a load cell of 1 kN was used to conduct tensile tests until breakage. The tests were conducted in accordance with the ASTM D882 methodology at room temperature, with a crosshead speed of 0.1 mm/min, under controlled displacement conditions. The applied force and specimen elongation were continuously recorded. The stress-strain curves were then obtained using the initial gauge length and cross section of each specimen. A rectangular sample measuring 5 cm × 2.5 cm was positioned between the tensile grips of the universal testing machine. To ensure consistency, this process was repeated for three identical samples. Statistical tests (ANOVA followed by a post hoc test) were conducted to assess the variation in mechanical properties based on different salt concentrations.

3. Results and discussion

3.1. FTIR spectroscopy study

FTIR spectroscopy is a valuable technique for predicting the interactions between polymer components within blends and between salt and polymer blends. This is achieved by analyzing the alterations in wavenumber and the intensities of the prominent bands. However, it is important to note that wavenumber changes within the resolution of the FTIR instrument, typically set at 4 cm^{-1}, were not considered. Observing these spectral changes provides valuable insights into the interactions occurring within polymer blends and their interactions with salts. The interaction between PVA and NaAlg has been previously discussed [14,15]. According to these reports, intermolecular hydrogen bonds exist between the $-OH$ group of PVA and the $-OH$ group/COO^- group of NaAlg polymer. The FTIR spectra of the $NaNO_3$ salt and salt-doped PVA-NaAlg blend are shown in Fig. 1.

According to Fig. 1, seven major bands corresponding to NaAlg/PVA blend system have been identified. $-OH$ stretching vibration at 3275 cm^{-1} [11,15,21], CH_2 asymmetric vibration at 2941 cm^{-1}[11,15,21], $C=O$ stretching vibration at 1710 cm^{-1}, asymmetric COO^- stretching vibration at 1594 cm^{-1}[13,21,22], symmetric COO^- stretching vibration at 1410 cm^{-1} [13,22,23], −CH wagging at 1262 cm^{-1} [22], and $-COC-$ stretching of the glycosidic bond at 1027 cm^{-1} [21]. The variation in these bands with increasing salt concentrations is discussed below. Assignments corresponding to the major bands of the salt-doped samples are listed in Table 2. It is clear from Table 2 that the wavenumber corresponding to the $-OH$ stretching has increased from 3275 cm^{-1} to 3368 cm^{-1}. This indicates the formation of coordination between the Na^+ cation and the O atom of the $-OH$ group of NaAlg and/or PVA Wavenumbers corresponding to $-OH$ bending in the pure blend are absent. This may indicate the formation of intermolecular hydrogen bonds between the $-OH$ group of PVA and the $-OH/COO^-$ group of NaAlg as previously mentioned [24]. Also, with the addition of salt, the band corresponding to −OH bending reappears and shows a decrease in wavenumber from 1376 cm^{-1} for PNN5 to 1351 cm^{-1} to PNN30. The reappearance of this band may indicate the ability of the salt to disrupt the inter-/intramolecular hydrogen bonds of the polymer blend [24]. The variation in wavenumber can be attributed to the formation of hydrogen bonds between the oxygen atom of the NO_3^- anion and the −

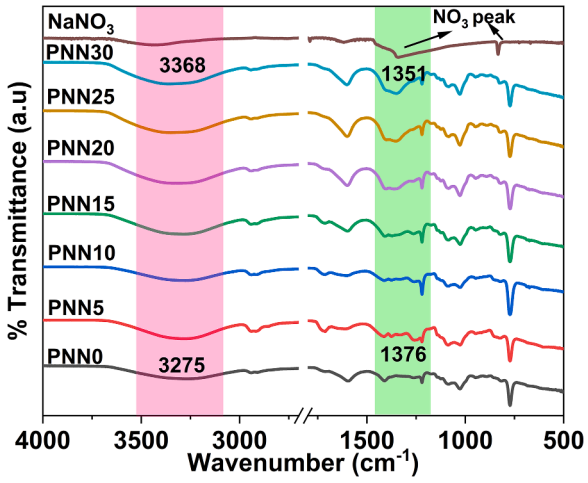

Fig. 1. FTIR spectra of $NaNO_3$ salt and NaAlg/PVA-$NaNO_3$ SPE system.

Table 2
FTIR band assignment for NaAlg/PVA-$NaNO_3$ SPE system.

Sample	Wavenumber of the prominent functional groups (cm^{-1})							
	O-H stretching	C-H_2 asymmetric stretching	C=O stretching	asymmetric COO- stretching	symmetric COO- stretching	OH bending	CH wagging	COC. stretching of the glycosidic bond
PNN0	3275	2941	1710	1594	1410	–	1262	1027
PNN5	3273	2940	1712	1595	1414	1376	1258	1026
PNN10	3276	2940	1712	1599	1412	1377	1260	1026
PNN15	3272	2942	1712	1598	1408	1372	1263	1026
PNN20	3340	2942	1712	1600	1403	1359	1267	1027
PNN25	3349	2941	1712	1601	1401	1352	–	1027
PNN30	3368	2943	1712	1602	–	1351	–	1028

OH group of NaAlg/PVA [25]. This is particularly true for the following reasons: $NaNO_3$ salt shows three prominent IR peaks: (i) $-OH$ band at 3500 cm^{-1} indicating moisture content, (ii) NO_3^- anion symmetric stretching at 1340 cm^{-1} and (iii) NO_3^- anion out of plane deformation mode at 832 cm^{-1} [26–28]. Since the NO_3^- anion peak overlaps with the peak of $-OH$ bending (i) a wavenumber shift in the $-OH$ bending band is seen, and (ii) an intensity change is observed in the region 1200 cm^{-1} to 1500 cm^{-1}. This further strengthens the interaction of the nitrate anion with the $-OH$ group.

Upon incorporation of $NaNO_3$ into the polymer matrix, the salt underwent dissociation, leading to the formation of Na^+ and NO_3^- ions. The Na^+ ion then establishes a dative bond (coordinate bond) through Lewis's acid-base interaction with the oxygen atom of the $-OH$ group. [25], whereas NO_3^- anion forms a hydrogen bond with the hydrogen atom of the $-OH$ group. Based on this analysis, the interaction between the salt and polymer matrix was substantiated, and the interaction scheme, as depicted in Fig. 2, was derived from the analysis of the FTIR spectra.

3.2. X-Ray diffraction (XRD)

The variation in the crystallinity of the blend polymer with increasing dopant concentration was evaluated using XRD. Fig. 3 shows the XRD spectra of the NaAlg/PVA-$NaNO_3$ system. The $NaNO_3$ salt shows sharp peaks at 2θ=29.5°, 31.6°, 35°, 38.6°, 42.3°, 47.8°, and several other high-angle peaks, indicating its crystalline nature. Such peaks were not present in the XRD spectra of PNN0 to PNN15, indicating the complete dissolution of salt in the polymer blend matrix. For the PNN30 sample, a salt peak at 2θ=29.5° ($NaNO_3$, JCPDS no. 36–1474) was superimposed on the XRD spectrum, indicating salt aggregation. The salt-free film (PNN0) displayed an amorphous nature with broad peaks centered at 2θ=13.8°and 20.0° [12]. The intensity of these peaks decreased, whereas the width of the peak increased, indicating an increase in the amorphous nature with salt loading, as per Hodge et al. criteria [29]. To quantify the variation in crystallinity, all XRD spectra were deconvoluted using a Gaussian function with the aid of the Fityk software [30] to reveal the crystalline and amorphous characteristics. Two-point baseline correction was performed prior to deconvolution [31], and a regression coefficient close to unity indicated the best fit to the original spectra. The degree of crystallinity was calculated using Eq. (7).

$$\chi_c = \frac{A_c}{A_T} \times 100\% \tag{7}$$

In Eq. (7), A_c is the total area under all crystalline peaks and A_T is the total area under both amorphous and crystalline peaks. Because the blend consisted of NaAlg and PVA, the deconvoluted peaks were assigned as crystalline/amorphous by considering the peaks from these components [12,32–34]. The deconvoluted spectra and corresponding crystallinity values are shown in Table 3.

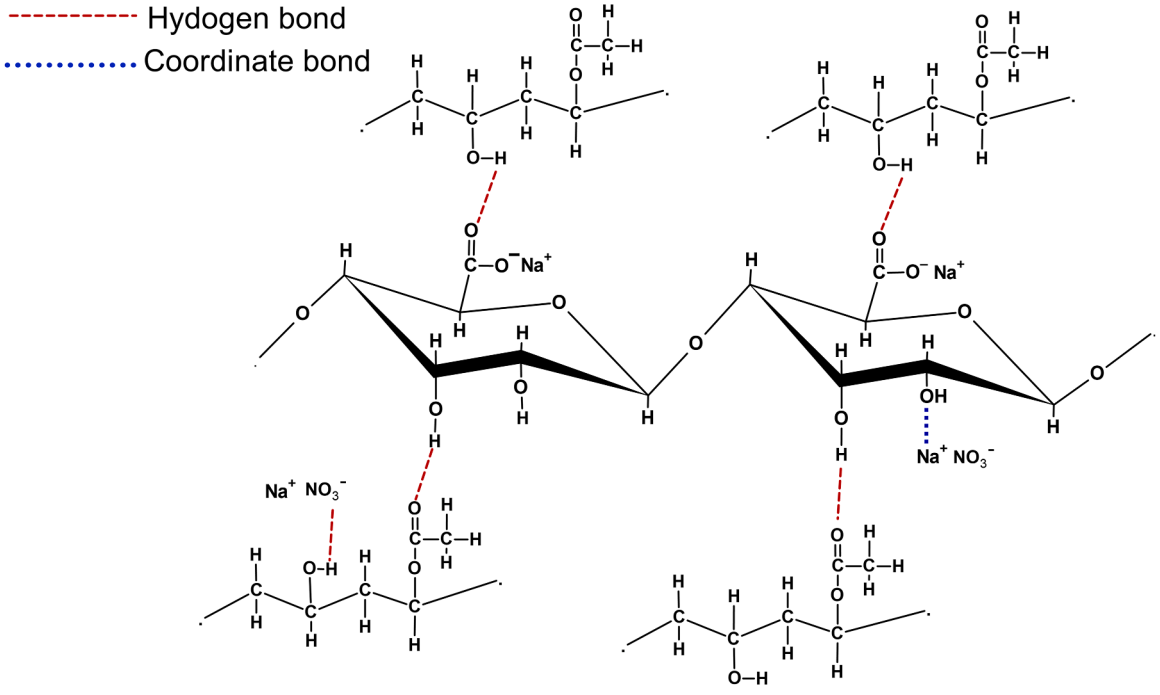

Fig. 2. Potential interaction pattern of $NaNO_3$ salt with NaAlg/PVA polymer blend inferred based on FTIR spectra.

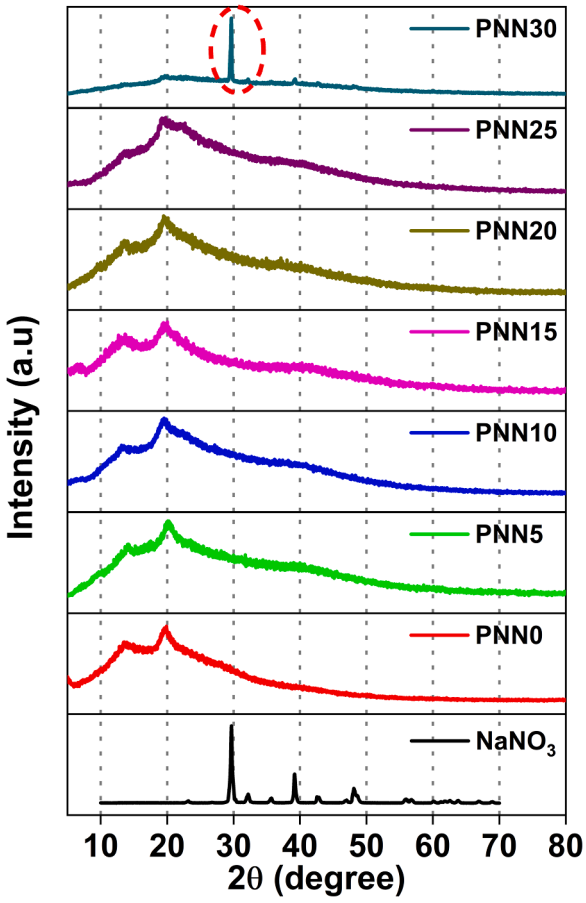

Fig. 3. XRD spectra for $NaNO_3$ salt and NaAlg/PVA-$NaNO_3$ SPE films.

As shown in Fig. 4 and Table 3, PNN15 was the most amorphous sample among all the samples, and for PNN20 and PNN25, the onset of salt crystallization was observed. For PNN30, additional crystalline peaks were observed (2θ=29.5°, 38.6°, and 42.3°), which accounted for the higher crystallinity of the sample due to the onset of salt recrystallization. In polymer electrolytes, ionic conduction is more favorable in the amorphous phase than in the crystalline phase. Therefore, PNN15 is expected to be the highest conducting sample among the doped samples.

3.3. Room temperature ionic conductivity

Fig. 5 shows the Nyquist plots (Z_r vs. $-Z_i$) obtained for various PNN samples at room temperature (25 °C). These plots exhibited a depressed semicircle in the high-frequency region and a tail in the low-frequency region. The presence of this tail is ascribed to the formation of a double layer at the electrolyte-electrode interface, which arises from the blocking behavior of stainless steel towards ions. The origin of the depressed semicircle observed in the high-frequency region can be attributed to a combination of factors. First, they arise from the resistance ions encountered in the bulk, hindering their flow. Second, polar groups within the polymer chains lead to the realignment of dipoles under the influence of an alternating field, resulting in capacitance. Thus, the depressed semicircle is a consequence of both the resistance to ion flow in the bulk and the capacitance arising from the dipole realignment within the polymer chains. An ideal Nyquist plot is expected to be a perfect semicircle followed by a spike parallel to the $-Z_i$ axis (Fig. 5(b)). The depressed semicircle instead of a perfect semicircle and the slanted tail instead of tails parallel to the $-Z_i$ axis may be due to the rough surface of the electrode/electrolyte and/or diffusion of charged species at the electrode/electrolyte interface (Fig. 5(c)). The bulk resistance R_b refers to the flow of ions that can be obtained by intersecting the semicircle with the Z_r axis. Electrical equivalent circuit (EEC) modeling was performed to further analyze the Nyquist plots. The EEC is selected based on the physical aspects that occur in the SS|PNN|SS cell during the impedance measurement. Based on the trend of the Nyquist plot in Fig. 5, the EEC consists of a constant phase element (CPE2, assigned to the tilted spike in the low-frequency region) in series with a parallel combination of another constant phase element (CPE1, assigned to the dipoles in bulk) and bulk resistance (R_b, assigned to the resistance to bulk ion flow). The latter is a parallel combination because the resistance to ion flow and bulk dipole realignment occur simultaneously. The EEC are shown in Fig. 5(b) and (c). A constant phase element (CPE) is chosen over the capacitor owing to the deviation of the Nyquist plot from ideal behavior. The CPE impedance equation is given by Eq. (8).

$$Z_{CPE} = \frac{k}{(j\omega)^p} \tag{8}$$

Here, k^{-1} is the capacitance of the CPE, and p is the fractional quantity ($0 < p < 1$) associated with the deviation of the spike from the vertical axis in the Nyquist plot. The dc conductivity is obtained using the relation

$$\sigma_{dc} = \frac{l}{R_b\, A} \tag{9}$$

where l is the thickness of the PNN samples and A is the effective contact area of the electrode/electrolyte surface.

The real (Z_r) and imaginary ($-Z_i$) parts of the impedance derived from EEC are as follows:

Table 3
Values of crystallinity, bulk resistance, R_b and dc conductivity, σ and Jonscher power law parameters for PNN samples at 25 °C.

Sample	Degree of crystallinity χ (%)	R_b (Ω)	σ (S cm^{-1}) at 25 °C	Dc conductivity at 25 °C from AC spectra (S cm^{-1})	Parameter B from Jonscher Fit	Parameter s from Jonscher Fit
PNN0	19.52	31218.20 ±762.27	(6.12±0.15) × 10^{-8}	(6.66±1.38) × 10^{-8}	8.88 × 10^{-13}	0.959
PNN5	7.56	9188.12 ±1892.91	(4.65±0.73) × 10^{-7}	(2.48±0.59) × 10^{-7}	7.82 × 10^{-12}	0.864
PNN10	7.06	4755.91±2.27	(8.03±0.03) × 10^{-7}	(8.40±0.46) × 10^{-7}	1.77 × 10^{-12}	0.802
PNN15	4.23	783.80±3.74	(6.50±0.03) × 10^{-6}	(6.42±0.63) × 10^{-6}	5.51 × 10^{-10}	0.653
PNN20	8.44	1801.12±29.99	(2.65±0.04) × 10^{-6}	(2.64±0.84) × 10^{-6}	3.37 × 10^{-12}	0.896
PNN25	8.52	5003.31±28.98	(7.63±0.04) × 10^{-7}	(7.78±0.78) × 10^{-7}	3.38 × 10^{-12}	0.950
PNN30	22.94	6821.80±36.20	(6.07±0.03) × 10^{-7}	(6.85±0.39) × 10^{-7}	2.18 × 10^{-12}	0.966

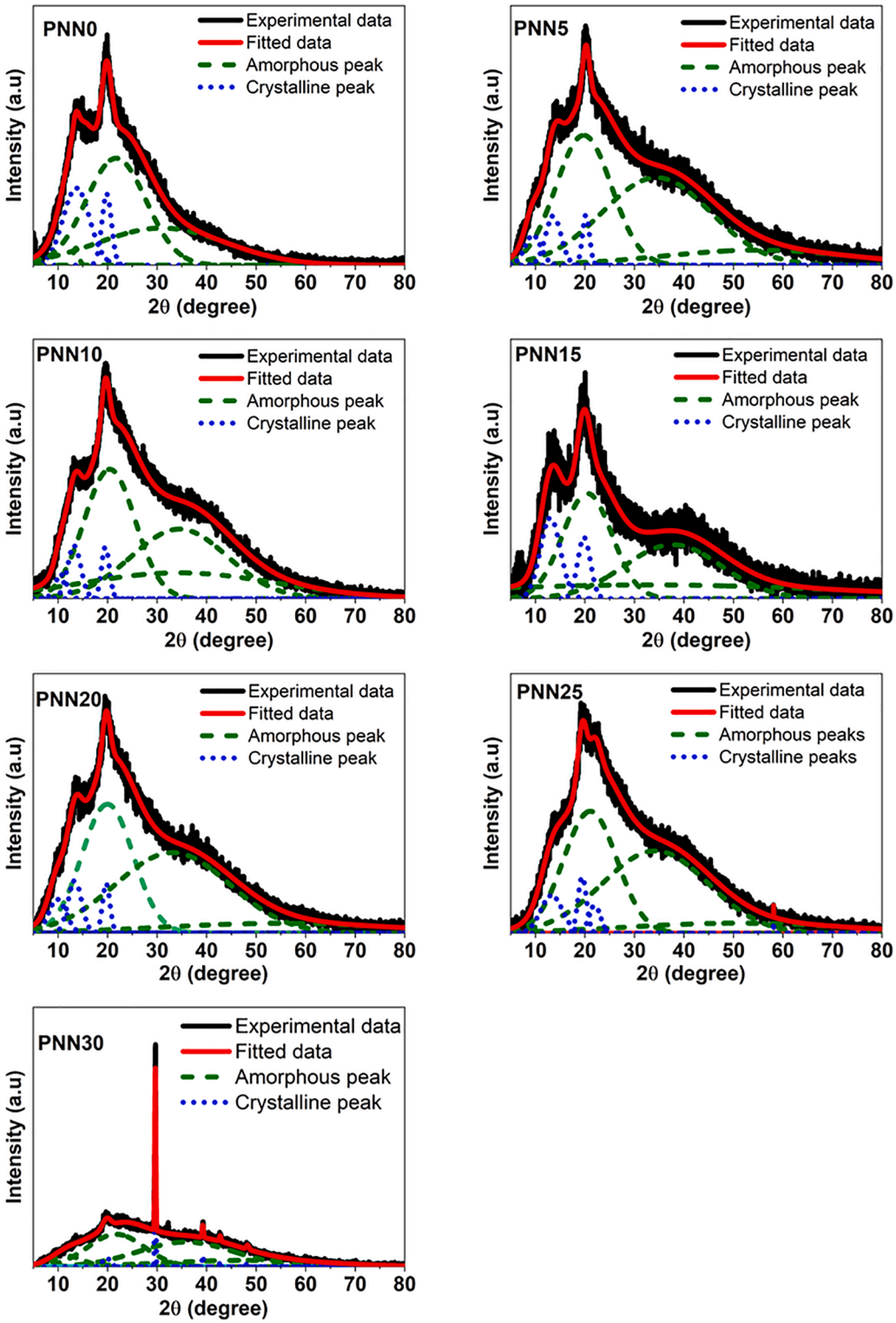

Fig. 4. Deconvoluted XRD pattern for NaAlg/PVA-$NaNO_3$ SPE films.

$$Z_r = \frac{R_b + R_b^2 k_1^{-1} \omega^{p_1} \cos\left(\frac{\pi p_1}{2}\right)}{1 + 2R_b k_1^{-1} \omega^{p_1} \cos\left(\frac{\pi p_1}{2}\right) + R_b^2 k_1^{-2} \omega^{2p_1}} + \frac{\cos\left(\frac{\pi p_2}{2}\right)}{k_2^{-1} \omega^{p_2}} \tag{10}$$

$$-Z_i = \frac{R_b^2 k_1^{-1} \omega^{p_1} \sin\left(\frac{\pi p_1}{2}\right)}{1 + 2R_b k_1^{-1} \omega^{p_1} \cos\left(\frac{\pi p_1}{2}\right) + R_b^2 k_1^{-2} \omega^{2p_1}} + \frac{\sin\left(\frac{\pi p_2}{2}\right)}{k_2^{-1} \omega^{p_2}} \tag{11}$$

Eqs. (10) and (11) were used to fit the Nyquist plot and deduce the bulk resistance value. The DC conductivities of each sample are presented in Table 3.

Table 3 provide results indicating that the direct current (dc) conductivity shows a noticeable increase upon doping and reaches its peak value for the PNN15 sample. This enhancement can be attributed to the amplified amorphous characteristics, as verified by XRD analysis. The increase in the amorphous nature was further supported by the reduction in bulk resistance as the salt concentration increased to 15 wt.%.

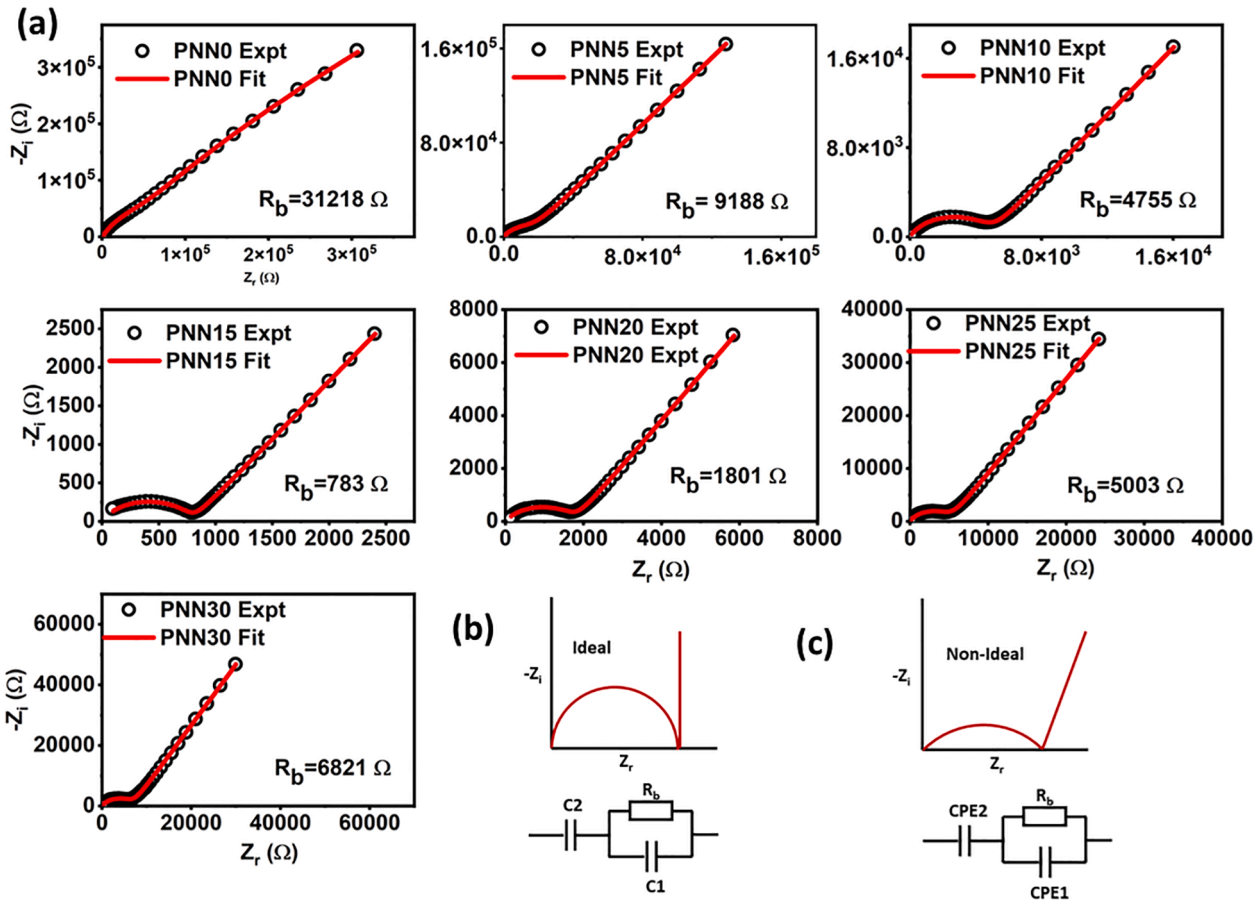

Fig. 5. (a) Nyquist plots for NaAlg/PVA-$NaNO_3$ SPE films, (b) ideal Nyquist plot and its EEC, and (c) non-ideal Nyquist plot along with its EEC.

However, the samples with salt concentrations exceeding 15 wt.% exhibit an increase in crystallinity, potentially caused by salt aggregation. This is corroborated by the degree of crystallinity data obtained from the XRD studies, as shown in Fig. 4.

The ionic conductivities of all the prepared samples at various temperatures (log σ versus 1000/T) from 308 K to 393 K are shown in Fig. 6.

The plot described here is linear. This suggests that the temperature dependence of the ionic conductivity $\sigma(T)$ obeys Arrhenius behavior described by the following equation:

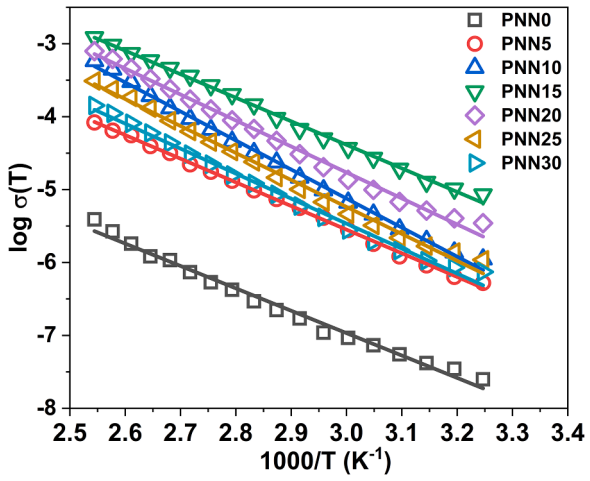

Fig. 6. Ionic conductivity-temperature plot showing Arrhenius behavior for the NaAlg-PVA-$NaNO_3$ SPE system.

$$\sigma(T) = \sigma_0 \exp\left(-\frac{E_a}{k_b T}\right) \tag{12}$$

In Eq. (12), σ_0 is the pre-exponential factor, E_a is the activation energy, k_b is the Boltzmann constant (k_b=1.38 × 10^{-23} JK^{-1}), and T is the temperature in Kelvin scale. Table 4 shows the ionic conductivity at 373 K, activation energy, and pre-exponential factor of the NaAlg-PVA-$NaNO_3$ electrolyte system. The Arrhenius model of conductivity involves hopping of ions between the coordinating sites decoupled from the polymer segmental motion[35]. The activation energy refers to the energy required for an ion to initiate its movement. In polymer electrolytes, the ion is typically "loosely bound" to a site where donor electrons are present. Once the ion attains sufficient energy, it can detach from the donor site and migrate to another donor site. This movement from one site to another facilitates charge conduction, and the energy required for this conduction is known as the activation energy. According to the Anderson-Stuart model[36], the activation energy is the combined energy of the ion's binding to its site and the kinetic energy required for migration. If the ion possesses sufficient energy to overcome the binding energy, it will dislocate from its site but remain within the same location. Only when the ion has an energy exceeding the binding energy, it will become a free ion capable of migrating to other locations.

As shown in Table 4, the activation energy increased substantially for lower concentrations of $NaNO_3$ salt (up to 10 wt.%). This suggests a decrease in the ionic conductivity if the pre-exponential factor remains nearly constant. However, experimentally, the conductivity values of the complex blend were at least two orders of magnitude higher than those of the uncomplexed blend. This increase in σ is due to a large increase in σ_0 as given in Table 4 [37,38]. However, the PNN15 sample had the lowest activation energy among the $NaNO_3$-doped samples,

Table 4
Variation of ionic conductivity at 373 K, activation energy (E_a) and pre-exponential factor (σ_0) obtained from the Arrhenius plot of the NaAlg-PVA-$NaNO_3$ system.

Sample	Conductivity Relaxation time τ ($\times 10^{-5}$ s)	Ionic conductivity at 373 K (S cm^{-1})	Pre-exponential factor σ_0	Activation energy (eV)	Regression coefficient R^2	Capacitance from imaginary modulus (pF)
PNN0	–	8.86×10^{-7}	175.14	0.609	0.988	78.245
PNN5	3.564	3.17×10^{-5}	1.51×10^{4}	0.645	0.998	89.328
PNN10	2.249	1.31×10^{-4}	6.64×10^{6}	0.790	0.996	67.477
PNN15	0.895	4.64×10^{-4}	1.99×10^{5}	0.641	0.997	98.473
PNN20	1.127	2.40×10^{-4}	8.41×10^{5}	0.707	0.993	65.413
PNN25	1.419	8.78×10^{-5}	7.22×10^{5}	0.734	0.992	64.351
PNN30	1.786	4.35×10^{-5}	6.58×10^{4}	0.680	0.993	86.927

showing its highest conducting properties. This was also evident from the conductivity values measured at 373 K. The increase in conductivity with salt concentration and temperature was investigated using transport parameter calculations, as outlined in the next subsection.

3.4. Dielectric analysis at room and elevated temperature

The ionic conductivity behavior of the NaAlg-PVA-$NaNO_3$ complex permittivity was studied as a function of the frequency and temperature. The complex permittivity has a real part ϵ' which indicates the stored energy, and an imaginary part ϵ'' which indicates energy loss due to periodic field reversals. As shown in Fig. 7(a) and (d), ϵ' increases as the salt concentration increases. This is because, as the salt concentration increases, more free ions are available in the system, and they accumulate at the electrode-electrolyte interface at a lower frequency, increasing the dielectric constant and hence the conductivity. Since the real part at low frequencies indicates the carrier concentration in the bulk of the electrolyte film, the same is been illustrated by the plot of the ϵ' at 100 Hz (Fig. 7(d)). Accordingly, PNN15 was the highest conducting sample, indicating that it had the highest number of free ions. This is consistent with the ε' trend obtained in Fig. 7(a), where PNN15 shows the highest dielectric constant, proving that a large amount of free ions accumulated at the electrode/electrolyte interface. Beyond 15 wt.%, the decrease of ϵ' implies a reduction in free ions in the system. This is due to "ion association." This occurs when the formation of an ion pair is more favorable than the formation of free ions. When there are more free ions, they begin to interact because of the small space in the polymer matrix. This leads to the formation of neutral ion pairs due to the Coulomb attractive force exerted between free cations and anions, leading to a reduction in ϵ' [39]. Furthermore, the graph of the imaginary part of the complex permittivity (Fig. 7(b)) as a function of the salt concentration indicates high values at low frequencies owing to the presence of more free ions. In this case, charges accumulate at the electrode-electrolyte interface because they have sufficient time to build up. However, as the frequency increases, owing to the high periodic field reversal rate, the ions do not have time to pile up, leading to a linear decrement in ϵ''. The sample with 15 wt.% salt shows the highest values of ϵ' and ϵ'' among the doped samples. Beyond 15 wt.%, ϵ'' drops due to ion polarization, as discussed earlier. In Fig. 7(c), the plot illustrates the change in *tanδ* with respect to the salt concentration. Notably, a peak was observed in the plot, indicating conductivity relaxation within the polymer samples. This peak emerges when the frequency of the rotating molecules aligns with the applied (AC) field. Correspondingly, the conductivity relaxation time (τ) has been calculated using the expression.

$$\tau = \frac{1}{2\pi f_{max}} \tag{13}$$

The values are presented in Table 4. The peak shifts towards higher

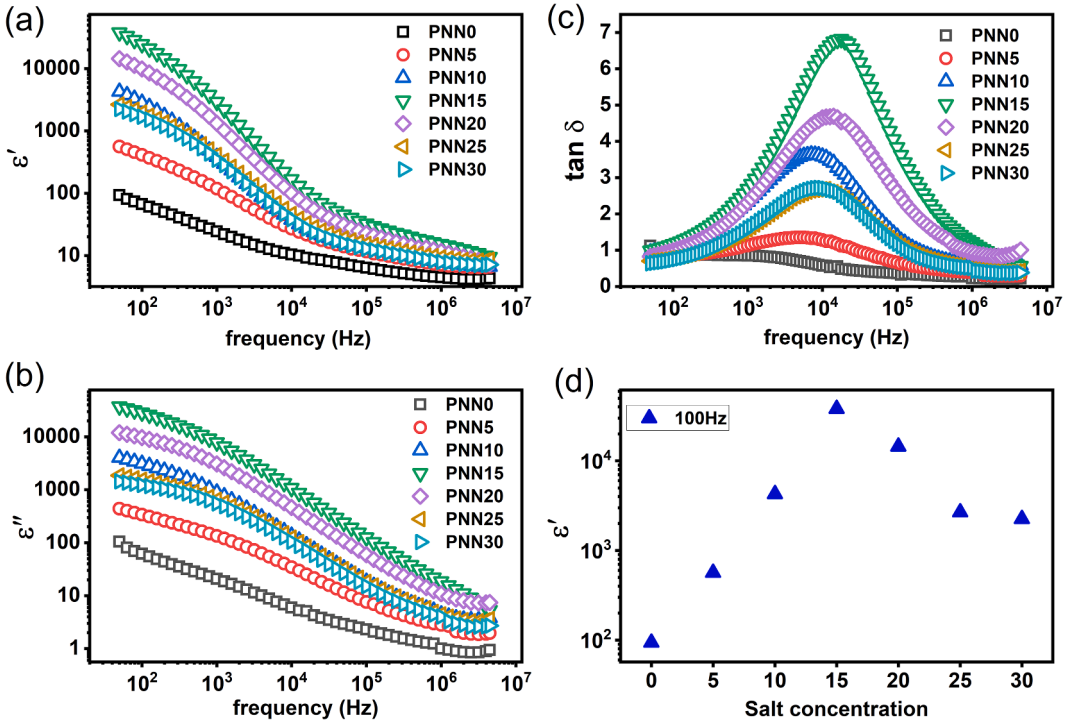

Fig. 7. Plot of (a) ε', (b) ε", (c)*tan δ*, (d) ϵ' at 100 Hz for NaAlg-PVA-$NaNO_3$ SPE system.

frequencies with salt concentrations up to 15 wt.% shows a reduction in the relaxation time, indicating a faster migration of ions from one site to another coordinating site [25]. This result explains the trend in the room-temperature conductivity obtained in Table 3, where the highest conductivity value obtained by PNN15 is due to faster ion migration. The increase in the peak height with increasing salt concentration indicates an increase in the carrier concentration [40].

The dielectric properties can vary depending on the applied frequency, temperature, and other properties of the polymer system. In this section, the effect of temperature on the dielectric properties of the optimum conducting sample PNN15 was studied at selected temperatures, as shown in Fig. 8.

Clearly ϵ' and ϵ'' increase with temperature due to the increase in the number of free ions with temperature. This is because, with sufficient energy, the salt breaks up to form free Na^+ and NO_3^- leading to more free ions in the system. This is related to Eq. (14).

$$n = n_0 \exp\left(-\frac{U}{\epsilon_r k_b T}\right) \tag{14}$$

Here n is the free carrier density, U is the salt dissociation energy, ϵ_r is the dielectric constant, $k_b$is the Boltzmann constant, and T is the temperature in Kelvin. There is no relaxation peak in the ϵ'', indicating no primary or secondary structural relaxation occurs in this given temperature range. Fig. 8(c) shows a plot of the tangent loss at the selected temperature. The presence of a non-symmetric peak around f_{max} suggests that the conductivity relaxation process departs from the typical exponential Debye behavior. Moreover, with increasing temperature, the graph shifted towards the higher frequency region, indicating a decreased conductivity relaxation time. This phenomenon can be attributed to the ionic charge carriers within the polymer material attempting to adjust to changes in the direction of the applied field, leading to variations in relaxation time. In addition to the shift of the peak towards higher frequencies, it was observed that the height of the peak increased. This increase in peak height suggested a decrease in the resistivity of the samples. The augmented peak height implies an increase in the carrier concentration within the samples, indicating a higher density of charge carriers available for conduction [41]. The variation of the relaxation time τ with temperature is shown in Fig. 8(d) and is found to be thermally activated as described by Arrhenius law

$$\tau = \tau_0 \exp\left(-\frac{E_D}{k_b T}\right) \tag{15}$$

Here τ_0 is the pre-exponential factor, E_D is the activation energy of the conductivity relaxation process, k_b is Boltzmann constant, and T is the temperature in kelvin. The activation energies were found to be 0.51 eV. This value is close to the activation energy obtained from the Arrhenius plot, indicating that the ions participating in the conduction are responsible for relaxation.

3.5. Modulus spectrum analysis at room and elevated temperature

The dielectric behavior of the NaAlg-PVA-$NaNO_3$ samples was investigated using modulus formalism. The real and imaginary parts of complex permittivity at room temperature (298 K) are shown in Fig. 9. At lower frequencies, M' and M'' show very low values due to the removal of electrode polarization (EP). With increased frequency, M' shows higher values at higher frequencies. The dispersion at higher frequencies is due to conductivity relaxation. This should be accompanied by a peak in M'' at higher frequencies, but it is not seen due to the limited frequency range [42].

The capacitance value is calculated based on the maximum values of M'' versus the frequency plot as

$$C = \epsilon_0 / 2M''_{max} \tag{16}$$

The values are listed in Table 4. These values were in the pF range, indicating bulk conduction. The PNN15 sample exhibited the highest capacitance of 98.73 pF. This is mainly due to the increased carrier concentration, leading to more ions available for double-layer formation, thereby giving rise to a high capacitance.

From Fig. 10(a) and (b), the temperature dependence of M' and M'' are shown for the PNN15 sample. Clearly, M' and M'' have longer tails at

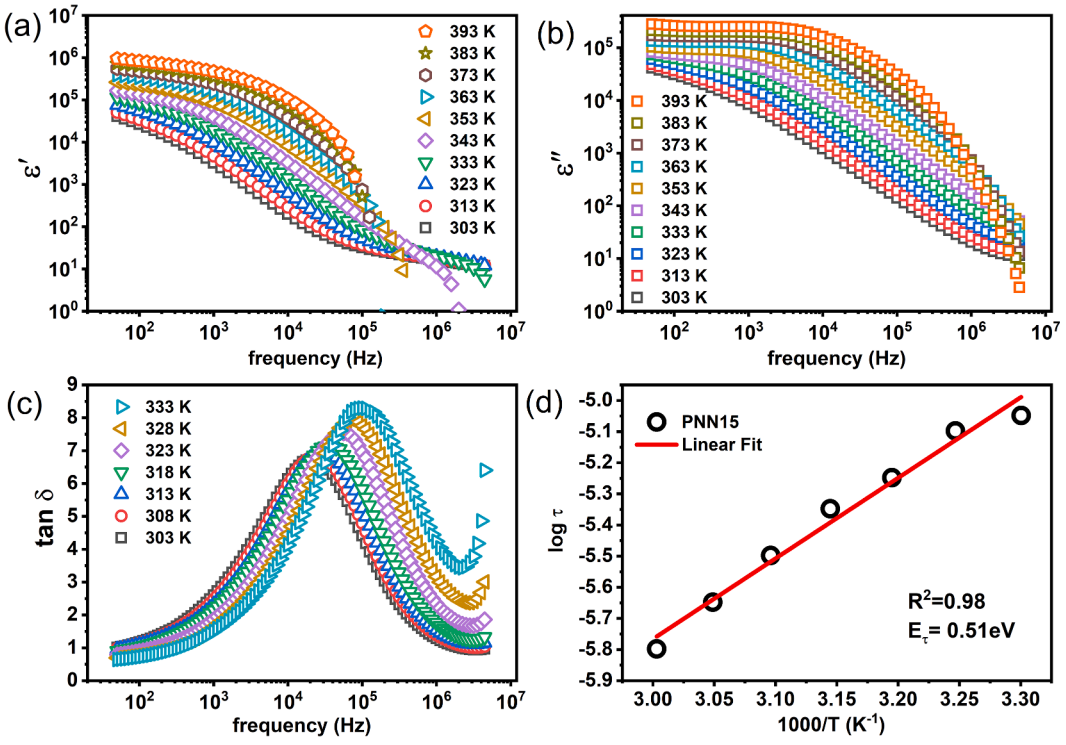

Fig. 8. Plot of (a) ϵ', (b) ϵ'', (c) $tan\delta$ and (d) log τ at selected temperatures for PNN15 sample.

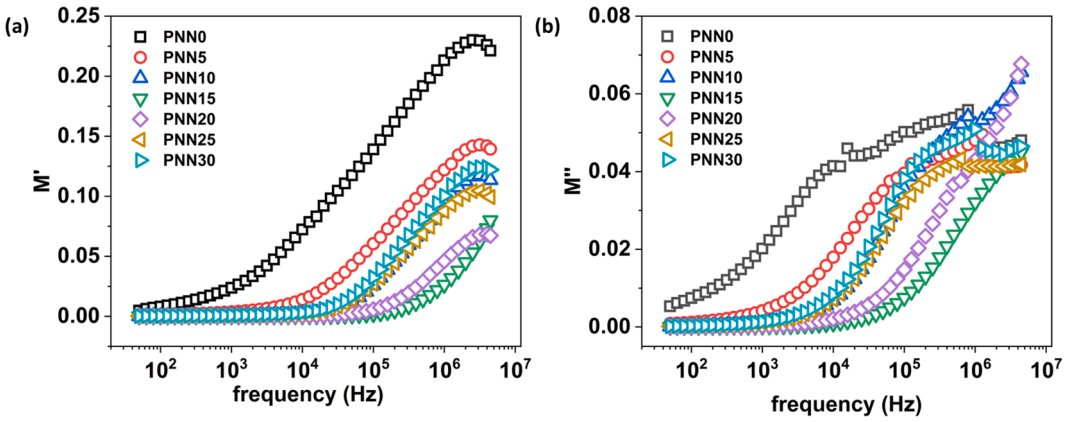

Fig. 9. Plots of (a) $M^{'}$ and (b) $M^{''}$ at room temperature for the NaAlg-PVA-$NaNO_3$ system.

low frequencies, and the peaks shift to the high-frequency side and are found to decrease steadily when the temperature is increased. This implies a reduction in relaxation time. The broad and asymmetric nature of the curve around the peak indicated a non-Debye nature. The observed non-Debye behavior can be attributed to multiple polarizations, relaxation mechanisms, and various interactions between the ions and dipoles within the system. The region to the right of the peak corresponds to carriers confined within the potential wells and exhibits mobility over short distances. This confinement leads to a dispersion in alternating current (AC) conductivity. However, the region to the left of the peak determines the range of charge carriers that can move over long distances. These carriers accumulate at the electrode/electrolyte interface and contribute to the electrode polarization (E.P) effect. The combination of these factors results in non-Debye behavior observed in the system. The Argand diagram is shown in Fig. 10(c). The incomplete semicircle implies a non-Debye nature [43]. The length of the arc observed in the $M^{'} - M^{''}$ curves is directly related to the conductivity of the polymer electrolyte. With increasing temperature, the arc length decreased, indicating an increase in conductivity. The arc behavior also provides valuable insights into the type of relaxation phenomenon that occurs, whether it is related to conductivity or viscoelastic relaxation. If the diameter of the arc in the $M^{'} - M^{''}$ curves align with the $M^{'}$ axis, it signifies the presence of a complete semi-circular arc. In such cases, a single relaxation time can be estimated, indicating that conductivity relaxation is consistent with the Debye model. However, if the $M^{'} - M^{''}$ curve exhibits partial semi-circular arcs. This implies a distributed relaxation time, and suggests that ion transport occurs through viscoelastic relaxation. The Argand plots in this study demonstrate incomplete semi-circular arcs, indicating the presence of a distribution of relaxation times, reflecting non-Debye properties. Consequently, ion transport in this system occurred via viscoelastic relaxation. [44]. Further, the capacitance at high temperatures is calculated by

$$C = \frac{1}{k_2^{-1}} \tag{17}$$

where k_2^{-1} is the double-layer capacitance formed at the electrode/electrolyte interface. This value was obtained by fitting the Nyquist plot

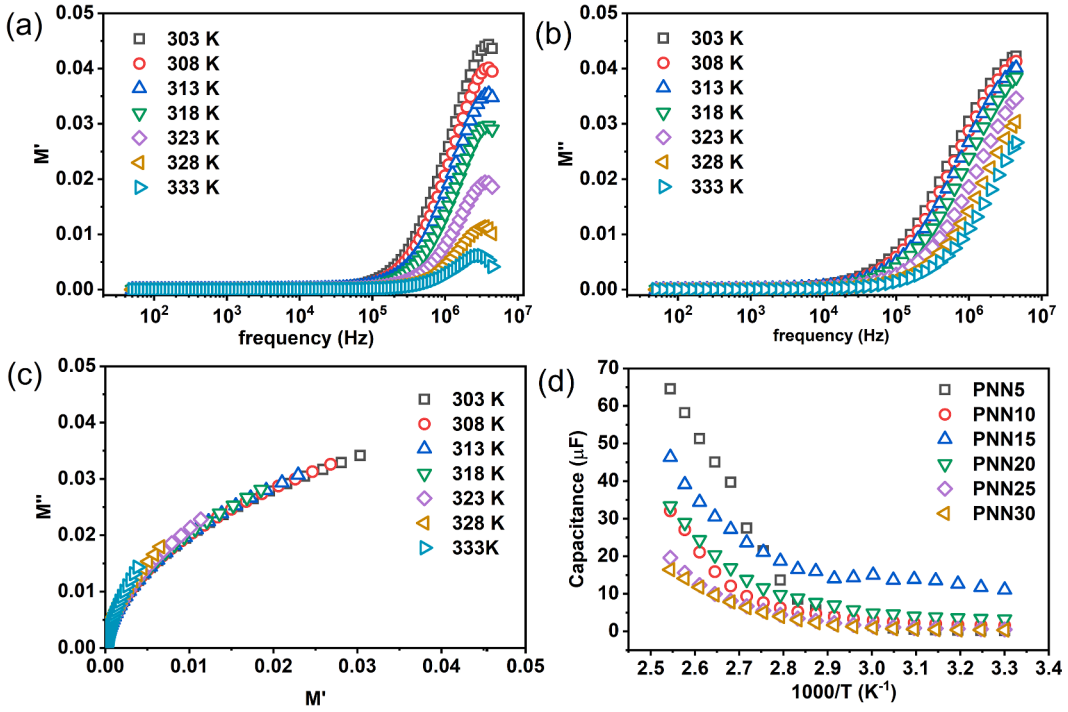

Fig. 10. Plot of (a)$M^{'}$, (b)$M^{''}$, (c) Argand diagram at selected temperatures for PNN15 sample and (d) capacitance as a function of temperature for doped NaAlg-PVA-$NaNO_3$ system.

using the EEC at high temperatures [39]. As shown in Fig. 10(d), the capacitance increased with temperature. This is because more ions are created as the temperature increases. Hence, more ions prevail at the electrode/electrolyte interface, leading to greater energy storage.

3.6. Ion transport properties at room and elevated temperatures

In this study, the charge carrier density (n), mobility (μ), and diffusion coefficient (D) of samples with various salt concentrations at room and elevated temperatures were investigated using the Arof-Noor method [45]. Accordingly, Nyquist plots were fitted using equations derived based on the EEC (Eq. 10 and (Eq. 11)). Using the fitted parameters, the ion transport parameters were estimated using the following equations:

$$D = \frac{e(k_2\varepsilon_r\varepsilon_0 A)^2}{\tau_2} \tag{18}$$

$$\mu = \frac{eD}{k_B T} \tag{19}$$

$$n = \frac{\sigma}{\mu e} \tag{20}$$

Here ε_r is the dielectric constant at the high frequency (1 MHz), k_B is the Boltzmann constant, T is the temperature in the Kelvin scale, and τ_2 is the value taken at the frequency corresponding to a $Z_i \rightarrow 0$. Fig. 11 shows the variation in the transport parameters as a function of salt concentration and ionic conductivity at room temperature for the NaAlg-PVA-$NaNO_3$ system.

As shown in Fig. 11, the room-temperature conductivity gradually increased as the salt concentration increased and reached an optimum value of 6.50×10^{-6} S cm^{-1} for 15 wt.% of the dopant. The conductivity then decreases beyond 15 wt.% and becomes 6.07×10^{-7} S cm^{-1} for 30 wt.% of dopant. The carrier concentration also followed this trend. This shows that more free ions (Na^+ and NO_3^-) are obtained when more salt is added. Hence, the higher carrier concentration of 15 wt.% of dopants. Beyond this dopant composition, the carrier concentration decreases because of the reassociation of free ions owing to the limited space between the ions. Therefore, the ionic conductivity decreases beyond 15 wt.%. This is particularly true since $\sigma = ne\mu$. A plot of n to μ ratio is constructed and presented in Fig. 12 to determine the predominant parameter that influences the ionic conductivity at room temperature.

The plot depicted in Fig. 12 exhibits a trend similar to that of the ionic conductivity. This observation leads to the conclusion that the carrier concentration significantly affects the ionic conductivity, surpassing the influence of the mobility and diffusion coefficient [46,47].

Now, the ion transport properties at elevated temperatures are discussed in detail.

Fig. 13 (a–c) shows the variation in the transport parameters as a function of temperature. The following characteristics were observed with temperature changes. As the temperature increased, n also increased. This is because the undissociated salt absorbs more energy

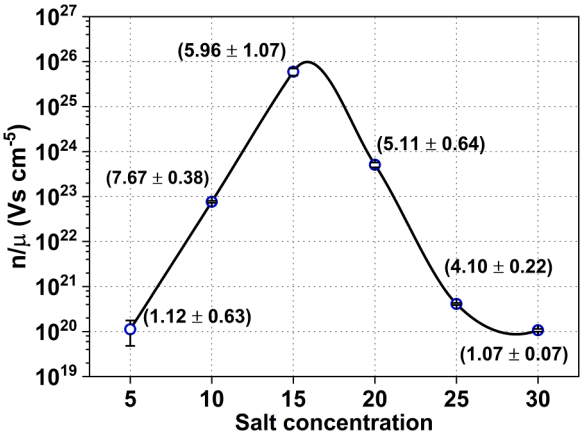

Fig. 12. Ratio of n to μ as a function of salt concentration at room temperature for NaAlg-PVA-$NaNO_3$ SPE system.

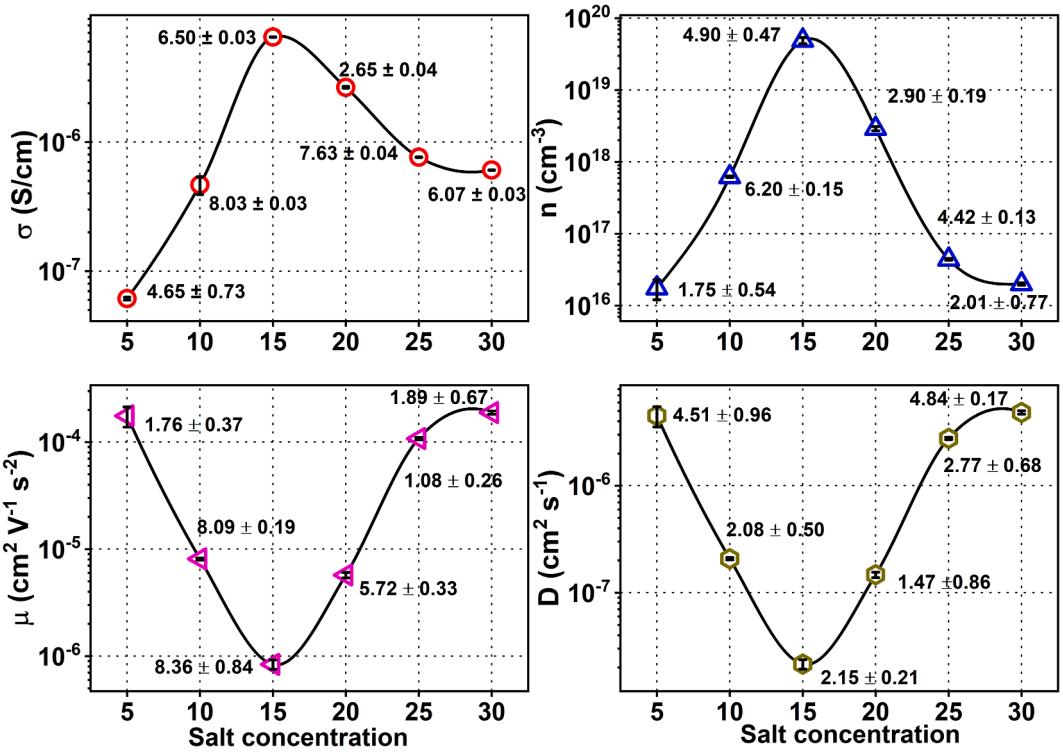

Fig. 11. Plot of ionic conductivity and transport parameters as a function of salt concentration at room temperature for the NaAlg-PVA-$NaNO_3$ SPE system.

from the heat when the temperature increases. Each atom in the undissociated salt vibrates at a high amplitude, leading to a decrease in the binding energy between the cation and anion, causing them to break into free ions [3]. PNN5 had a very high carrier concentration at very high temperatures, followed by PNN15. The abrupt increase in PNN5 carrier concentration at high temperatures may be due to the low salt concentration in the sample. At high temperatures, more free ions were formed. Based on the Ideal gas law, an increase in the temperature increases the volume of the polymer matrix. Electrolytes with low salt concentrations can maximize salt dissociation. Compared to the sample with a high salt concentration, the number of free ion dissociations should also be higher than in an electrolyte with a low salt concentration; however, in this case, the free ions sit close to each other because of the large number of free ions filling the space. This event leads to the formation of ion associations, resulting in low *n*. The increased carrier concentration of PNN5 resulted in a lower mobility and diffusion coefficient owing to the increased ion collision owing to the limited space available for carrier movement. A similar decrease in *n* and μ is seen in the case of the PNN30 sample up to some temperature.

Moreover, PNN5 and PNN30 had high crystallinity, which was three times higher than that of the other samples. The high crystallinity may cause a reduction in the free volume, facilitating a lower carrier mobility in these samples. This is mainly due to the increase in the Stokes drag coefficient, as shown in Fig. 13(d) [48]. The Stokes drag coefficient is calculated as

$$F_d = \frac{k_b T}{D} \tag{21}$$

Here, k_b is the Boltzmann constant, T is the absolute temperature, and $D$is the diffusion coefficient, whose value is obtained from Nyquist plot fitting.

The Stokes drag coefficient is related to the amorphousness and viscosity of a polymer matrix. Increasing the Stokes drag coefficient implies a higher viscosity, leading to slower carrier motion [39]. For samples (other than PNN5 and PNN30), the increase in mobility can be caused by the high energy of the charge carriers obtained owing to the increase in thermal energy. As per Table 4, the ionic conductivity value of the PNN15 sample at 100 °C is the highest among all the samples despite having a lower *n* when compared to PNN5. Thus, the increase in conductivity at elevated temperatures for PNN15 is influenced not only by the carrier concentration but also by the mobility.

3.7. Concentration and temperature-dependent ac conductivity studies

Fig. 14 shows the real part of the complex conductivity, revealing three distinct regions. The first region, the low-frequency dispersion region, is characterized by faster ion migration and electrode polarization. The second region is a frequency-independent plateau region that appears at a slightly higher frequency than that of the low-frequency dispersion region. The third region corresponds to long-range ionic

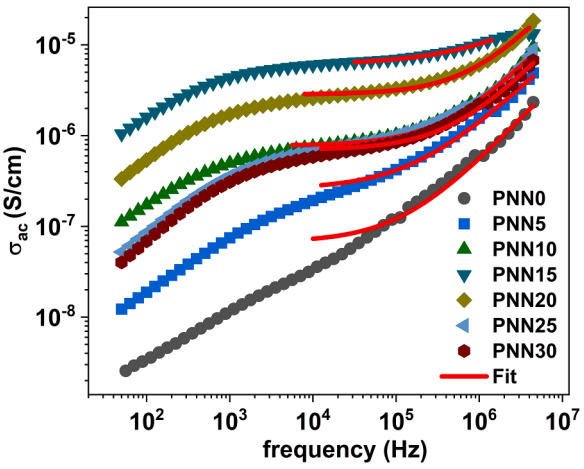

Fig. 14. AC conductivity spectra for NaAlg/PVA-$NaNO_3$ SPE films.

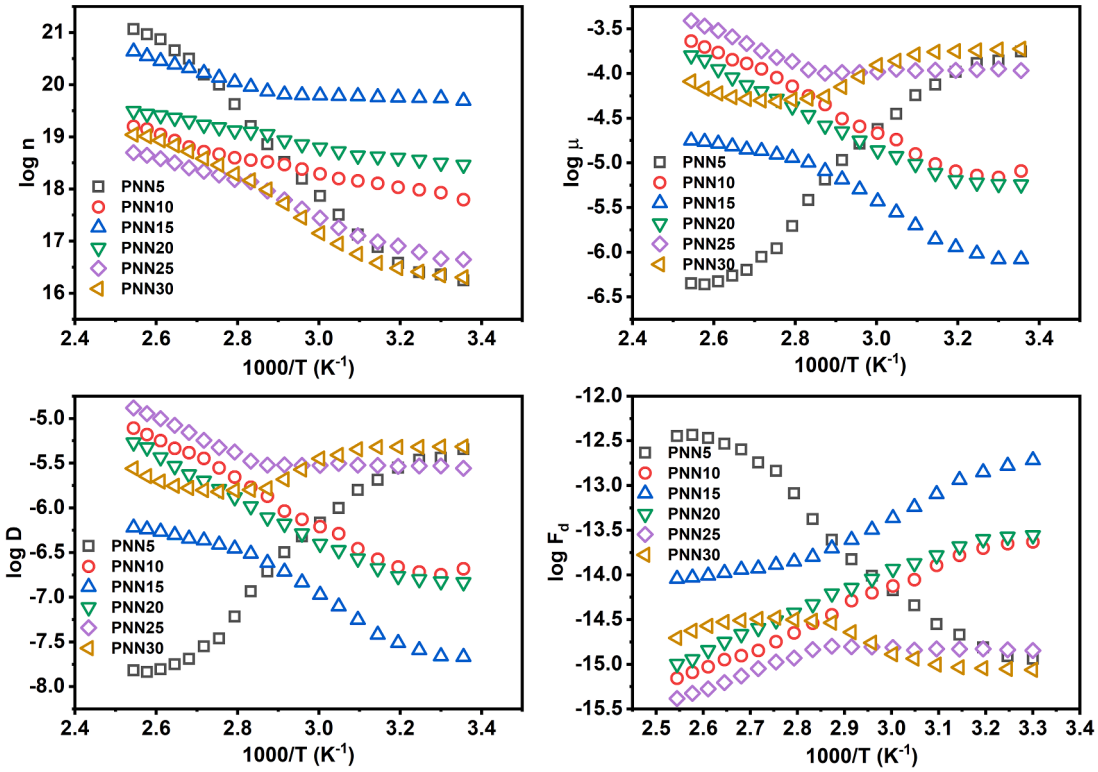

Fig. 13. Plot of (a-c) transport parameters and (d) Stokes drag coefficient at various temperatures for NaAlg-PVA-$NaNO_3$ SPE system.

motion, representing the direct-current (DC) conductivity, followed by the high-frequency dispersion region. The high-frequency dispersion region is associated with short-range ionic motion, often called hopping. The DC conductivity can be determined by extrapolating the mid-frequency region to the *y*-axis at ω=0. Conductivity curves usually follow a power law, starting from the Jonscher power law

$$\sigma_{ac} = \sigma_{dc} + B\omega^{s} \tag{22}$$

In Eq. 22, the exponent is restricted to $s < 1$, to an augmented power law with $s > 1$ also allowed. Exponent *s* is related to the ion dynamics in each frequency range. As the frequency increases, the ion motion passes from free hopping ($s = 0$), to correlated hopping ($0 < s < 1$), followed by confined ion motion ($s > 1$) [49]. The power law formalism is suitable for fitting the mid- and high-frequency regions, excluding the low-frequency dispersion region. The low-frequency dispersion region is attributed to electrode polarization, which arises from the double layer formed at the electrode-electrolyte interface. It is important to note that the choice of electrode played a crucial role in this phenomenon. However, the low-frequency dispersion region is often disregarded or not considered in a focused discussion of ion dynamics. Jonscher's power law, as described by Eq. (22), consists of two terms. The first term is temperature-dependent and represents the DC conductivity. It dominates at both low and high temperatures. The second term is both frequency- and temperature-dependent and is associated with the dielectric relaxation of the carriers. It dominates at high frequencies and low temperatures [50]. Constant *B* is a temperature-dependent parameter with conductivity units, and *s* is an exponent between 0 and 1. According to Funke's jump relaxation model [51], the exponent *s* is defined as

$$s = \frac{back\ hop\ rate}{site\ relaxation\ time} \tag{23}$$

If *s* is less than unity, the backward hop is slower than the site relaxation, leading to translational motion of Na^{+} ions. The AC conductivity spectra were fitted using the equation given by nonlinear least square fitting, and the parameters are listed in Table 3. The dc conductivity obtained by the fitting method matches the values obtained from the Nyquist plot formalism and "s" is in the range of 0.65–0.96 for the salt-doped samples. Poorly conducting samples have higher values of "s" indicating small fraction of ions are participating in conduction process[52].

Several theoretical models have been proposed to explain the relationship between the exponent "s" and temperature in polymer electrolytes. These models help to elucidate the conduction mechanism in such systems. The most relevant models include (1) Quantum Mechanical Tunnelling (QMT): According to the QMT model, the exponent "s" remains independent of temperature. (2) Small polaron quantum mechanical Tunnelling (SP): In the SP model, conduction is predominant when the exponent "s" increases with the temperature.

(3) Correlated Barrier Hopping (CBH): CBH model predicted a decrease in the exponent "s" as the temperature increased. (4) Overlapping Large Polaron Quantum Mechanical Tunnelling (OLP): In the OLP model, the exponent "s" is expected to decrease with increasing temperature until it reaches a minimum and then begins to increase again. By comparing the variation of "s" with temperature to these theoretical models, it becomes possible to gain insights into the specific conduction mechanism in the polymer electrolyte system.

The variation in exponent *s* as a function of temperature for the highest conducting sample (PNN15) from 303 K to 343 K is shown in Fig. 15(b). Above 338 K, the Jonscher fit did not converge. Hence, the *s* value was not calculated (Fig. 15(a)). In our case, because the value of *s* is equal to 1 and does not depend on the temperature, the conduction mechanism in the PNN15 sample follows the QMT model in the studied temperature range.

3.8. Differential scanning calorimetry (DSC)

The variation of the glass transition temperature (T_g) with salt concentration probed by DSC. DSC thermograms for all samples from 25 °C to 200 °C are shown in Fig. 16. The midpoint of the step transition under the broad endotherm appears around 30 °C to 120 °C gives T_g. The glass transition temperature for the pure blend is approximately 52.5 °C and is found to increase when salt is added and reaches a maximum of 74.8 °C for PNN15. Subsequently, it was found to decrease with increasing salt concentration. The elevation in T_g can be explained based on the number of free Na^{+} ions. Based on the study of the transport properties, the carrier concentration increases with the salt content and is maximum in the PNN15 electrolyte. Due to salt aggregation, the carrier concentration decreases with salt content beyond that PNN15 composition. The increase in T_g with salt concentration is due to the transient crosslink between the Na^{+} ion and the O atom of the -O.H. group, as indicated by FTIR studies [53]. The more free ions, the higher the T_g value. As the carrier concentration decreases beyond PNN15, T_g is found to decrease. This is because the formation of salt aggregation has reduced the number of free ions and interrupted the formation of transient crosslink between the Na^{+} ion and the O atom of -OH group, leading to a decrement in T_g [54].

3.9. Thermogravimetric analysis (TGA)

Thermal stability is an important parameter for electrolytes in energy storage devices as it determines the operating temperature range. The corresponding TGA and DTG curves of the NaAlg/PVA-$NaNO_3$ samples are shown in Fig. 17 in the temperature range of 25 °C and 500 °C. Three decomposition stages were observed in this temperature range. The initial mass loss occurs because of moisture loss from the samples that may have accumulated during sample handling for testing [55]. The

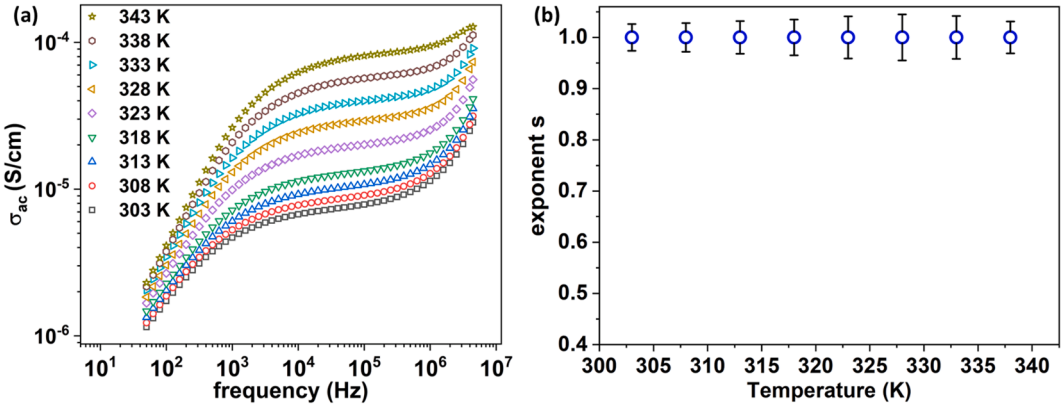

Fig. 15. (a) A.C conductivity spectra at selected temperatures and (b) variation in exponent *s* for NaAlg/PVA-15 wt.% $NaNO_3$ SPE films.

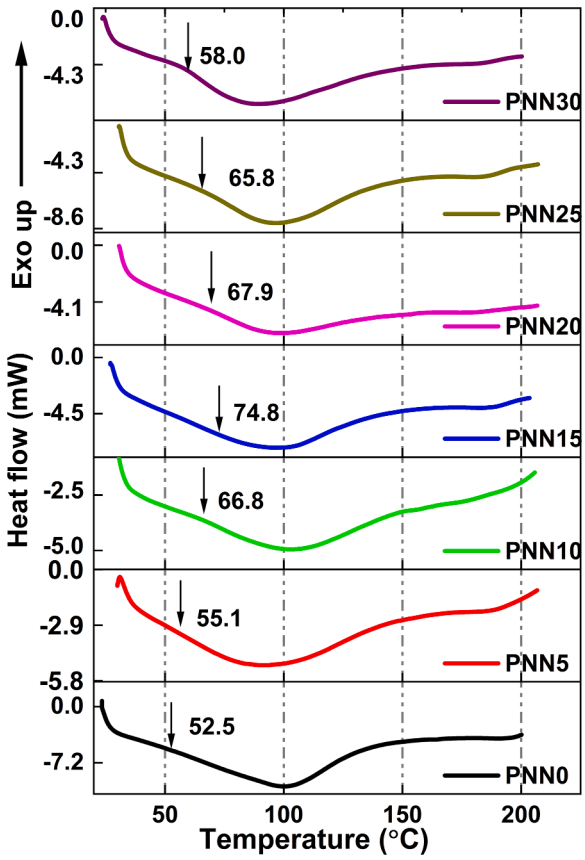

Fig. 16. DSC thermogram for NaAlg/PVA-$NaNO_3$ PBE films.

maximum degradation of the samples occurred in the temperature range 200–300 °C. This refers to the breakdown of glycosidic bonds in NaAlg and the loss of hydroxyl groups, leading to a mass loss of approximately 45% [56,57]. When there are multiple peaks observed in the major decomposition in the Differential Thermogravimetry (DTG) curve, the extrapolated onset temperature is commonly selected as the maximum decomposition temperature, denoted as T_d. This extrapolated onset temperature represents the temperature at which the decomposition process begins and provides a measure of the maximum decomposition temperature of the analyzed sample. By selecting the extrapolated onset temperature as T_d, it allows for a consistent and standardized approach in determining the maximum decomposition temperature in cases where multiple peaks are present in the DTG curve. The third stage of mass loss was observed at approximately 350 °C and 450 °C, which represents the decomposition of the remaining carbon residue.

As shown in Table 5, the thermal stability of the sample was lower than that of the pure blend. Moreover, the percentage of mass loss was higher for PNN15 than that for PNN0. This can be attributed to the weakening of the glycosidic bonds due to the interaction of Na^+ with the O atom, leading to a decrease in T_d as discussed in FTIR and DSC studies. However, from the perspective of energy storage devices, the thermal stability of the highest-conducting sample is sufficient for its operation, as it can operate up to 210 °C.

3.10. Field emission scanning electron microscopy (FESEM)

The SEM images at 20 μm resolution and 1kX magnification for selected samples (PNN0-PNN25) are shown in Fig. 18. PNN0 (salt-free film) showed a uniform morphology without any porous structure, indicating good miscibility of NaAlg and PVA as a blend component. With the inclusion of $NaNO_3$ salts, morphological changes were observed in samples with different degrees of roughness [58,59]. For the PNN5 sample, small and unequal-sized pores were observed owing to salt complexation. The pore size appeared to increase further for the PNN10 sample. These pores help improve the transport of Na^+ ions by increasing the surface area, which helps in ion diffusion through the polymer and increases its overall conductivity [60,61]. The pores became large and merged with one another for PNN15, indicating the most amorphous nature of the films among all the doped samples [62–64]. This observation supports the degree of crystallinity calculated from the XRD diffractogram, which shows that PNN15 is the most amorphous sample. For the PNN20 and PNN25 samples, large chunks of salts were observed, which indicates that salt aggregation in the films inhibits the overall conductivity of these samples [65]. This is supported by the trend of room temperature conductivity in Fig. 11, where the conductivity of PNN20 drops to $(2.65\pm0.04) \times 10^{-6}$ S cm^{-1} from $(6.50 \pm0.03) \times 10^{-6}$ S cm^{-1} and again drops to $(7.63\pm0.04) \times 10^{-7}$ S cm^{-1} in PNN25. The agglomeration of salt observed in the PNN25 sample was confirmed by the non-uniform distribution of sodium and nitrogen, as seen in the elemental mapping (Fig. 19). The SEM studies support the data obtained from the XRD and impedance studies, where crystallinity increased and conductivity decreased beyond the PNN15 samples. Thus, the SEM studies show that the PNN15 sample is the most amorphous among the doped samples.

3.11. Linear sweep voltammetry (LSV)

The electrochemical stability window (ESW) defines the operating potential range of a battery cell. In this work, linear sweep voltammetry (LSV) was used to determine the ESW of the prepared SPEs. The current in the LSV experiment initially remained near zero until the applied potential reaches a threshold value. When the voltage exceeds this threshold, the current abruptly increases, signifying the start of the electrochemical process. To maximize energy density and performance of batteries, the ESW of a SPE should be wide, which is beyond the cutoff potential of cathode materials in batteries. In many situations, an ESW of 3 V to 4 V is considered optimal [66]. Referring to Fig. 20, it is observed that the ESW for the highest conducting sample is 2.92 V. This value is a reasonable ESW for Na battery applications [67,68].

3.12. Transference number measurement (TNM)

Transference number measurement (TNM) allows the identification of the dominant charge carriers within the sample. To assess the behavior of the NaAlg/PVA-$NaNO_3$ electrolyte system, the *I-t* characteristics were observed over time. A constant direct current (DC) potential of 0.5 V was applied to a symmetric cell comprising salt-doped samples placed between two stainless steel (S.S.) electrodes (see Fig. 21). Notably, the electrodes used in this setup blocked ions. Initially, the current comprises contributions from both the electrons and ions. However, the final current originates solely from electrons [76]. The total ionic transference number (t_{ion}) and the electronic transference number (t_{elec}) is calculated with the following equations:

$$t_{ion} = 1 - \frac{I_f}{I_{in}} \tag{24}$$

$$t_{elec} = 1 - t_{ion} \tag{25}$$

Using the transference number and bulk conductivity (σ) obtained from E.I.S. measurements, the ionic (σ_{ion}) and electronic conductivities $(\sigma_{electronic})$ can be estimated using Eqs. (26) and (27).

$$\sigma_{ionic} = t_{ion} \times \sigma \tag{26}$$

$$\sigma_{electronic} = t_{elec} \times \sigma \tag{27}$$

The calculated total ionic transference numbers and ionic-electronic conductivities are listed in Table 6.

A total ionic transference value close to 1 indicates that the primary

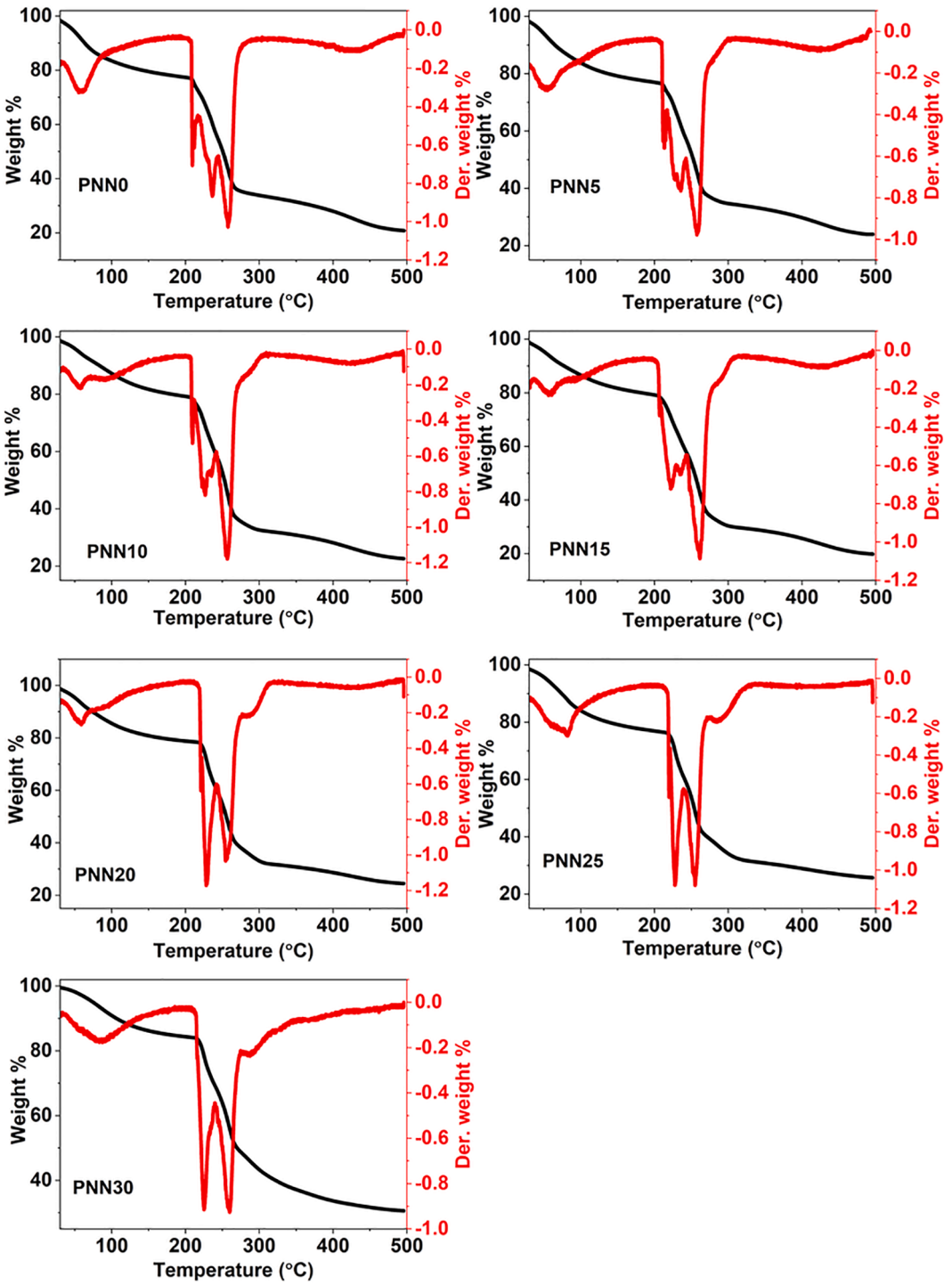

Fig. 17. TGA and DTG curves for NaAlg/PVA-$NaNO_3$ SPE films.

Table 5
Thermal parameters for NaAlg/PVA-$NaNO_3$ SPE films.

Sample	Maximum decomposition temperature T_d (°C)	Percentage of mass loss (%)
PNN0	223.96	45.17
PNN5	225.32	43.94
PNN10	214.87	48.85
PNN15	211.28	50.92
PNN20	222.84	47.75
PNN25	222.01	47.15
PNN30	219.12	41.45

carrier is an ion. Hence, the ionic current is maximal, and the electronic current is minimal, meeting the criteria for an energy storage device.

3.13. Mechanical properties

The mechanical properties of a solid polymer electrolyte are crucial because they directly affect the suppression of dendrite formation, ultimately enhancing safety [69,70]. Many metrics exist, but the tensile test reported here is the most common. Tight polymer networks responsible for the higher mechanical strength are responsible for the lower polymer mobility and, consequently, lower ion motion. Therefore,

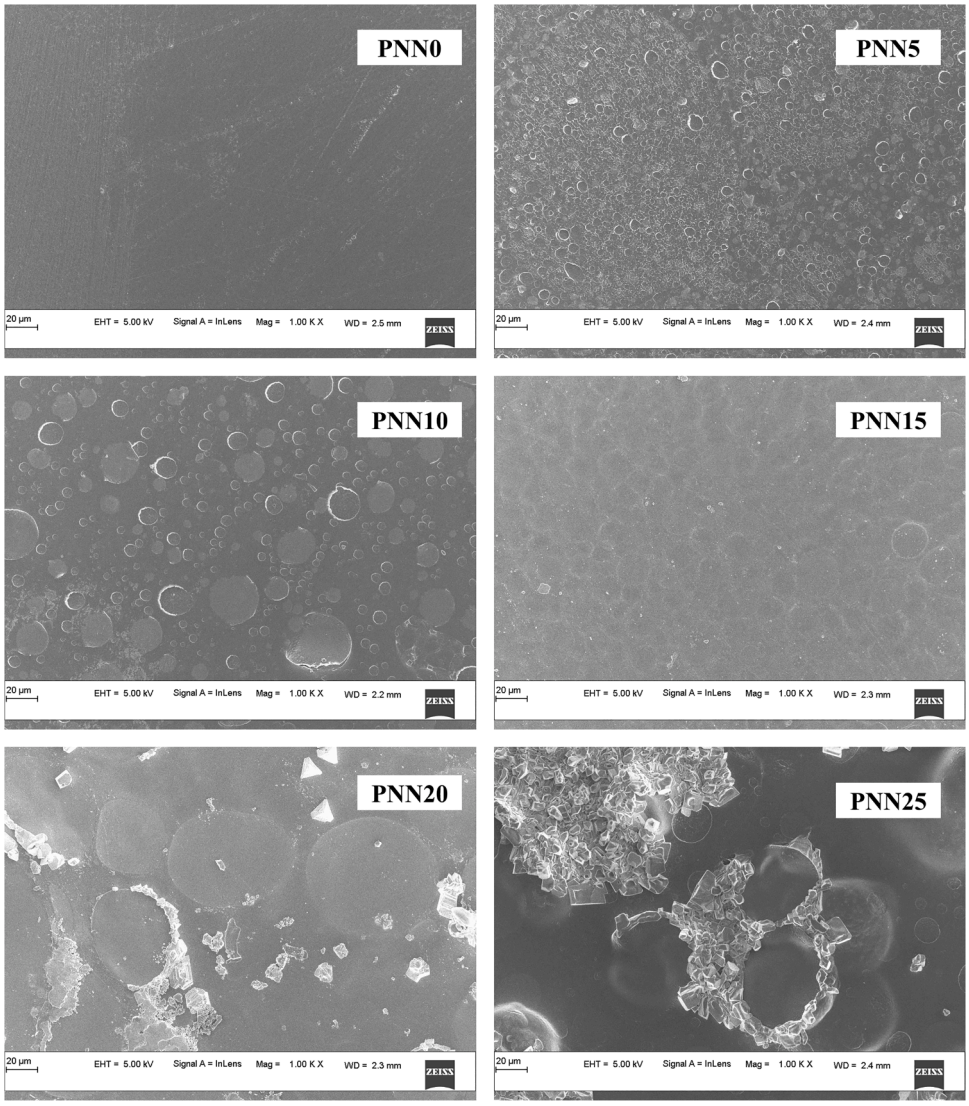

Fig. 18. SEM images for NaAlg/PVA-$NaNO_3$ SPE films.

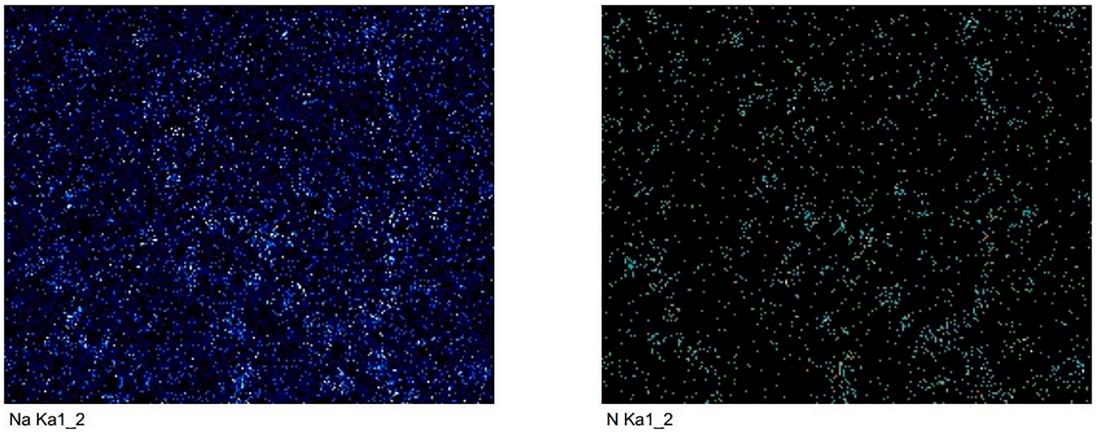

Fig. 19. Elemental mapping of PNN25 sample describing the distribution of Na and N in the sample.

it is difficult to achieve a high ionic conductivity and tensile strength [2]. The stress-strain curve, along with the changes in parameters such as tensile strength, Young's modulus, and elongation at break in relation to salt concentration, are depicted in Fig. 22. Table 7 lists all values obtained from Fig. 22.

The typical tensile strengths of sodium-based solid polymer electrolytes (SPEs) vary within the range of 1.5 MPa to 40 MPa[71–74]. Establishing a benchmark for tensile strength in solid polymer

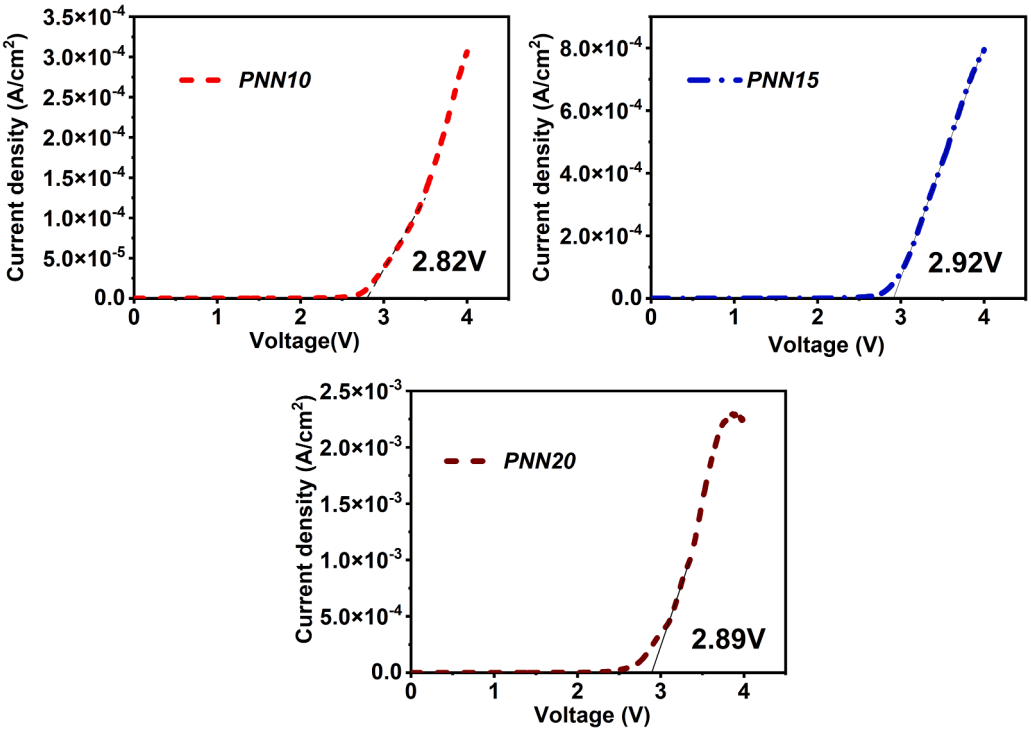

Fig. 20. LSV curves for NaAlg/PVA-$NaNO_3$ SPE films.

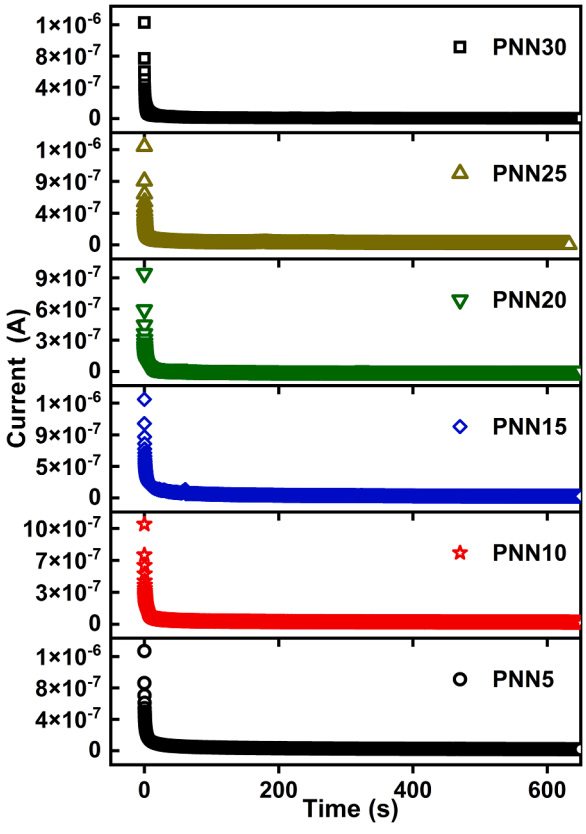

Fig. 21. *I-t* characteristics of the NaAlg/PVA-$NaNO_3$ SPE system.

electrolytes (SPEs) can be challenging because of the wide range of values observed. According to Table 7, the tensile strength falls within the range of 25 MPa to 45 MPa, which can be considered as a reasonable range for SPEs. As shown in Fig. 22(b), the tensile strength did not vary

Table 6
Variation of total ionic transference number, electron transference number, ionic conductivity, and electronic conductivity of NaAlg/PVA-$NaNO_3$ samples.

Sample	t_{ion}	t_{elec}	σ_{ionic}(S cm^{-1})	$\sigma_{electronic}$(S cm^{-1})
PNN5	0.985	0.015	5.267×10^{-7}	8.021×10^{-9}
PNN10	0.985	0.015	5.777×10^{-7}	8.797×10^{-9}
PNN15	0.982	0.018	2.016×10^{-6}	3.696×10^{-8}
PNN20	0.997	0.003	1.138×10^{-6}	3.426×10^{-9}
PNN25	0.995	0.005	1.159×10^{-7}	5.822×10^{-10}
PNN30	0.996	0.004	6.821×10^{-8}	2.739×10^{-10}

significantly ($p<0.05$) with the salt. The elongation at break values for PNN0 to PNN10 varies between 1 and 4% making them unsuitable for many practical applications. Table 7 shows that the values of elongation at break improved as the salt concentration increased. This suggests more favorable molecular interactions within the polymer film [75].

4. Conclusions

SPEs based on NaAlg-PVA blend polymers complexed with various concentrations of $NaNO_3$ were successfully prepared. The Nyquist plot fitting method was used to evaluate the transport parameters of the NaAlg-PVA-$NaNO_3$ SPEs in the temperature range 323–393 K. The room temperature conductivity increased from $(6.12\pm0.15) \times 10^{-8}$ S cm^{-1} (PNN0) to a maximum of $(6.50\pm0.03) \times 10^{-6}$ S cm^{-1} (PNN15). Subsequently, the conductivity decreases. The increase in conductivity at room temperature was primarily influenced by the carrier concentration rather than its mobility. As the temperature increased, the conductivity of all the samples showed an upward trend. Under these conditions, both the mobility and carrier concentration play significant roles in governing the electrolyte conductivity. The changes in conductivity at room temperature were influenced by the decrease in crystallinity, as observed by X-ray diffraction (XRD). This reduction in crystallinity was attributed to the interaction between a substantial number of Na^+ ions and the oxygen atoms of the -OH group and NO_3^- ions and the hydrogen atoms of the -OH group, as evidenced by the FTIR spectra. The

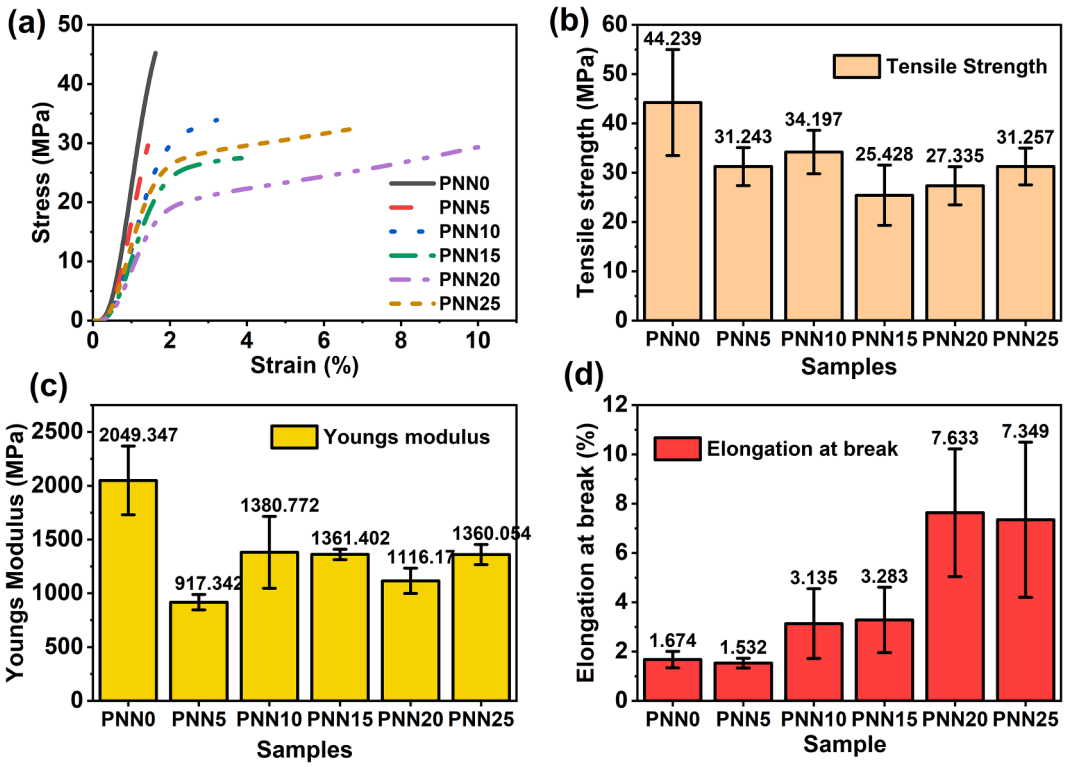

Fig. 22. (a) Stress-strain graph and variation of (b) tensile strength, (c) Young's modulus, and (d) elongation at the break for NaAlg/PVA-$NaNO_3$ SPEs.

Table 7
Mechanical properties of NaAlg/PVA-$NaNO_3$ SPEs.

Sample	Tensile strength (MPa)	Elongation at break (%)	Young's modulus (MPa)
PNN0	44.239±10.753	1.674±0.331	2049.347±319.733
PNN5	31.243±3.854	1.532±0.196	917.342±71.970
PNN10	34.197±4.404	3.135±1.417	1380.772±334.926
PNN15	25.428±6.100	3.283±1.328	1361.402±48.341
PNN20	27.335±3.872	7.633±2.592	1116.17±117.769
PNN25	31.257±3.716	7.349±3.147	1360.054±93.564

fluctuations observed in the glass transition temperature were attributed to the temporary crosslinks formed between the salts and functional groups of the polymer. The sample with the highest conductivity (PNN15) had the highest electrochemical stability window (ESW) of 2.92 V. The same samples exhibited good mechanical properties. Although the optimal conducting sample has sufficient ESW and sufficient mechanical strength, it lacks high ionic conductivity ($< 10^{-4}$ S cm^{-1}), making it unsuitable for energy storage device applications. Therefore, increasing the conductivity by incorporating nanofillers/plasticizers into the optimally conducting sample is necessary to realize technological applications. Further analyses should be conducted to improve the current electrolyte system.

CRediT authorship contribution statement

Vipin Cyriac: Conceptualization, Methodology, Data curation, Investigation, Writing – original draft. **:** Methodology, Investigation, Validation, Resources, Writing – review & editing, Supervision. **Y.N. Sudhakar:** Visualization, Resources, Data curation, Investigation. **Kuldeep Mishra:** Data curation, Visualization, Resources. **Z.E. Rojudi:** Data curation, Formal analysis. **M.S. Murari:** Visualization, Resources. **I.M. Noor:** Formal analysis, Writing – review & editing.

Declaration of Competing Interest

The authors declare that they have no known competing financial interests or personal relationships that could have appeared to influence the work reported in this paper.

Data availability

Data will be made available on request.

Acknowledgments

Vipin Cyriac expresses gratitude to the Directorate of Minorities, Bengaluru, Government of Karnataka, for their financial support in the form of the *Directorate of Minorities Fellowship for Minority Students*. The authors would like to thank Dr. Saraswati. Masti, Department of Chemistry, Karnataka Science College, Dharwad, Karnataka, India, for providing the UTM for mechanical property measurements.

References

[1] D.E. Fenton, J.M. Parker, P.V. Wright, Complexes of alkali metal ions with poly (ethylene oxide), Polymer 14 (1973) 589, https://doi.org/10.1016/0032-3861(73)90146-8 (Guildf).
[2] F. Gebert, J. Knott, R. Gorkin, S. Chou, S. Dou, Polymer electrolytes for sodium-ion batteries, Energy Storage Mater. 36 (2021) 10–30, https://doi.org/10.1016/j.ensm.2020.11.030.
[3] N.A. Abdul Aziz, E.Z.M. Tarmizi, C.S.C. Razak, I.M. Noor, Impact of charge carrier transport properties on conductivity-temperature dependence of gellan gum-LiCF3SO3 biopolymer electrolyte, High Perform. Polym. 34 (2022) 691–700, https://doi.org/10.1177/09540083221102743/ASSET/IMAGES/LARGE/10.1177_09540083221102743-FIG2.JPEG.
[4] R. Shogren, D. Wood, W. Orts, G. Glenn, Plant-based materials and transitioning to a circular economy, Sustain. Prod. Consum. 19 (2019) 194–215, https://doi.org/10.1016/J.SPC.2019.04.007.
[5] M. George, T.E. Abraham, Polyionic hydrocolloids for the intestinal delivery of protein drugs: alginate and chitosan — a review, J. Control. Release 114 (2006) 1–14, https://doi.org/10.1016/J.JCONREL.2006.04.017.

[6] M. Xie, F. Zhang, L. Liu, Y. Zhang, Y. Li, H. Li, J. Xie, Surface modification of graphene oxide nanosheets by protamine sulfate/sodium alginate for anti-cancer drug delivery application, Appl. Surf. Sci. 440 (2018) 853–860, https://doi.org/10.1016/J.APSUSC.2018.01.175.

[7] M. Infanta Diana, D. Lakshmi, P. Christopher Selvin, S. Selvasekarapandian, Substantial ion conduction in the biopolymer membrane: efficacy of NaI on sodium alginate matrix, Mater. Lett. 312 (2022), https://doi.org/10.1016/j.matlet.2022.131652.

[8] M.I. Diana, P.C. Selvin, S. Selvasekarapandian, M.V. Krishna, Investigations on Na-ion conducting electrolyte based on sodium alginate biopolymer for all-solid-state sodium-ion batteries, J. Solid State Electrochem. 25 (2021) 2009–2020, https://doi.org/10.1007/s10008-021-04985-z.

[9] D.R. Paul, Polymer blends, Journal of Macromolecular Science—Reviews in Macromolecular Chemistry 18 (1) (1980) 109–168.DOI, https://doi.org/10.1080/00222358008080917.

[10] N.M. Ghazali, N.F. Mazuki, A.S. Samsudin, Characterization of biopolymer Blend-based on alginate and Poly(vinyl Alcohol) as an application for polymer host in polymer electrolyte, Materials Today: Proceedings, Volume 48, Part 4, 2022, Pages 849-853, ISSN 2214-7853, 10.1016/j.matpr.2021.02.401.

[11] Tuncer Çaykara & Serkan Demirci (2006) Preparation and Characterization of Blend Films of Poly(Vinyl Alcohol) and Sodium Alginate, Journal of Macromolecular Science, Part A, 43:7, 1113-1121, DOI: 10.1080/10601320600740389.

[12] J.M. Yang, N.C. Wang, H.C. Chiu, Preparation and characterization of poly(vinyl alcohol)/sodium alginate blended membrane for alkaline solid polymer electrolytes membrane, J. Memb. Sci. 457 (2014) 139–148, https://doi.org/10.1016/j.memsci.2014.01.034.

[13] S. Safi, M. Morshed, S.A. Hosseini Ravandi, M. Ghiaci, Study of electrospinning of sodium alginate, blended solutions of sodium alginate/poly(vinyl alcohol) and sodium alginate/poly(ethylene oxide), J. Appl. Polym. Sci. 104 (2007) 3245–3255, https://doi.org/10.1002/APP.25696.

[14] T. Sheela, R.F. Bhajantri, P.M.G. Nambissan, V. Ravindrachary, B. Lobo, J. Naik, S. G. Rathod, Ionic conductivity and free volume related microstructural properties of LiClO4/PVA/NaAlg polymer composites: positron annihilation spectroscopic studies, J. Non Cryst. Solids 454 (2016) 19–30, https://doi.org/10.1016/J.JNONCRYSOL.2016.10.010.

[15] T. Sheela, R.F. Bhajantri, V. Ravindrachary, P.K. Pujari, S.G. Rathod, Preparation and characterization of NaClO4 doped poly(vinyl alcohol)/sodium alginate composite electrolyte, AIP Conf. Proc. (2013) 1302–1303, https://doi.org/10.1063/1.4791531. , American Institute of PhysicsAIP, Department of Physics, Mangalore University, Mangalagangotri - 574 199, India.

[16] Sheela, T., et al. "Ionic conductivity studies in crystalline PVA/NaAlg polymer blend electrolyte doped with alkali salt KCl." *AIP Conference Proceedings*. Vol. 1591. No. 1. American Institute of Physics, 2014. 10.1063/1.4872544.

[17] S. Shenbagavalli, M. Muthuvinayagam, S. Jayanthi, M.S. Revathy, Investigations on Al2O3 dispersed PEO/PVP based Na+ ion conducting blend polymer electrolytes, J. Mater. Sci. Mater. Electron. 32 (2021) 9998–10007, https://doi.org/10.1007/s10854-021-05658-3.

[18] A.A. Pritam, A.L. Sharma, Dielectric relaxations and transport properties parameter analysis of novel blended solid polymer electrolyte for sodium-ion rechargeable batteries, J. Mater. Sci. 54 (2019) 7131–7155, https://doi.org/10.1007/s10853-019-03381-3.

[19] T. Sreekanth, M. Jaipal Reddy, S. Ramalingaiah, U.V. Subba Rao, Ion-conducting polymer electrolyte based on poly (ethylene oxide) complexed with NaNO3 salt-application as an electrochemical cell, J. Power Sources 79 (1999) 105–110, https://doi.org/10.1016/S0378-7753(99)00051-8.

[20] M. Sadiq, S. Tanwar, M.M.H. Raza, S.M. Aalam, M. Sarvar, M. Zulfequar, A. L. Sharma, J. Ali, High performance of the sodium-ion conducting flexible polymer blend composite electrolytes for electrochemical double-layer supercapacitor applications, Energy Storage 4 (2022) e345, https://doi.org/10.1002/EST2.345.

[21] N.M.J.J. Rasali, Y. Nagao, A.S. Samsudin, Enhancement on amorphous phase in solid biopolymer electrolyte based alginate doped NH4NO3, Ionics (Kiel) 25 (2019) 641–654, https://doi.org/10.1007/s11581-018-2667-3.

[22] S. Zhang, H. Dandan, D. Zongxian, W. Xin, Z. Dan, H.U. Yan, X. Xincai, Fabrication and characterization of one interpenetrating network hydrogel based on sodium alginate and polyvinyl alcohol, (n.d.).(2023) 10.1007/s11595-019-2112-0.

[23] N.A.M. Zain, M.S. Suhaimi, A. Idris, Development and modification of PVA–alginate as a suitable immobilization matrix, Process Biochem. 46 (11) (2011) 2122–2129, https://doi.org/10.1016/j.procbio.2011.08.010.

[24] C. Chavan, R.F. Bhajantri, V. Cyriac, S.S.B. Ismayil, K. Sakthipandi, Investigations on anomalous behavior of ionic conductivity in NaPF6 salt loaded hydroxyethyl cellulose biodegradable polymer electrolyte for energy storage applications, Polym. Adv. Technol. (2023), https://doi.org/10.1002/PAT.6004.

[25] V. Cyriac, Ismayil, I.S.B.M. Noor, Z.E. Rojudi, Y.N. Sudhakar, C. Chavan, R. F. Bhajantri, M.S. Murari, Modification in the microstructure of sodium carboxymethylcellulose/polyvinyl alcohol polyblend films through the incorporation of NaNO3 for energy storage applications, Int. J. Energy Res. 46 (2022) 22845–22866, https://doi.org/10.1002/er.8588.

[26] Z. Ren, X. Xu, X. Wang, B. Gao, Q. Yue, W. Song, L. Zhang, H. Wang, Raman FTIR, XPS analysis during phosphate, nitrate and Cr(VI) removal by amine cross-linking biosorbent, J. Colloid Interface Sci. 468 (2016) 313–323.

[27] S. Bourahla, A.Ali Benamara, S.Kouadri Moustefai, Infrared spectra of inorganic aerosols: ab initio study of (NH 4)2SO4, NH4NO3, and NaNO3, Can. J. Phys. 92 (2014) 216–221, https://doi.org/10.1139/cjp-2013-0367.

[28] C. Ehrhardt, M. Gjikaj, W. Brockner, Thermal decomposition of cobalt nitrato compounds: preparation of anhydrous cobalt(II)nitrate and its characterisation by Infrared and Raman spectra, Thermochim. Acta 432 (2005) 36–40.

[29] R.M. Hodge, G.H. Edward, G.P. Simon, Water absorption and states of water in semicrystalline poly(vinyl alcohol) films, Polymer 37 (1996) 1371–1376, https://doi.org/10.1016/0032-3861(96)81134-7 (Guildf).

[30] M. Wojdyr, S. Gierlotka, B. Palosz, FITYK – peak-fitting software with support for powder patterns analysis, Acta Crystallogr. A 60 (2004) s246, https://doi.org/10.1107/S010876730409511X. –s246.

[31] W. Yao, Y. Weng, J.M. Catchmark, Improved cellulose X-ray diffraction analysis using Fourier series modeling, Cellulose 27 (10) (2020) 5563–5579, https://doi.org/10.1007/S10570-020-03177-8, 27 (2020).

[32] L. Marangoni Júnior, R.G. da Silva, C.A.R. Anjos, R.P. Vieira, R.M.V. Alves, Effect of low concentrations of SiO2 nanoparticles on the physical and chemical properties of sodium alginate-based films, Carbohydr. Polym. 269 (2021), 118286, https://doi.org/10.1016/J.CARBPOL.2021.118286.

[33] F.H. Abd El-Kader, W.H. Osman, H.S. Ragab, A.M. Shehap, M.S. Rizk, M.A. F. Basha, Electrical and Optical Properties of Polyvinyl Alcohol Thin Films Doped with Metal Salts, J. Polym. Mater. 21 (2004) 49–60.

[34] I.S. Noor, S.R. Majid, A.K. Arof, Poly(vinyl alcohol)–LiBOB complexes for lithium–air cells, Electrochim. Acta 102 (2013) 149–160, https://doi.org/10.1016/J.ELECTACTA.2013.04.010.

[35] S.B. Aziz, T.J. Woo, M.F.Z. Kadir, H.M. Ahmed, A conceptual review on polymer electrolytes and ion transport models, J. Sci. Adv. Mater. Devices 3 (2018) 1–17, https://doi.org/10.1016/j.jsamd.2018.01.002.

[36] O.L. ANDERSON, D.A. STUART, Calculation of activation energy of ionic conductivity in silica glasses by classical methods, J. Am. Ceram. Soc. 37 (1954) 573–580, https://doi.org/10.1111/J.1151-2916.1954.TB13991.X.

[37] S. Chandra, S.A. Hashmi, G. Prasad, Studies on ammonuim perchlorate doped polyethylene oxide polymer electrolyte, Solid State Ion. 40–41 (1990) 651–654, https://doi.org/10.1016/0167-2738(90)90090-E.

[38] K.K. Maurya, N. Srivastava, S.A. Hashmi, S. Chandra, Proton conducting polymer electrolyte: II poly ethylene oxide + NH4l system, J. Mater. Sci. 27 (23) (1992) 6357–6364, https://doi.org/10.1007/BF00576285, 27 (1992).

[39] K.L. Chai, M.M. Aung, I.M. Noor, H.N. Lim, L.C. Abdullah, Observation of ionic conductivity on PUA-TBAI-I2 gel polymer electrolyte, Sci. Rep. 12 (1) (2022) 1–20, https://doi.org/10.1038/s41598-021-03965-7, 12 (2022).

[40] T. Winie, A.K. Arof, Dielectric behaviour and AC conductivity of LiCF3so3 doped H-chitosan polymer films, Ionics 10 (2004) 193–199, https://doi.org/10.1007/BF02382816/METRICS (Kiel).

[41] S. Ramesh, R. Shanti, E. Morris, Discussion on the influence of DES content in CA-based polymer electrolytes, J. Mater. Sci. 47 (2012) 1787–1793, https://doi.org/10.1007/S10853-011-5964-Z/METRICS.

[42] S.B. Aziz, Z.H.Z. Abidin, Ion-transport study in nanocomposite solid polymer electrolytes based on chitosan: electrical and dielectric analysis, J. Appl. Polym. Sci. 132 (2015), https://doi.org/10.1002/APP.41774.

[43] R.M. Hill, L.A. Dissado, Debye and non-Debye relaxation, J. Phys. C Solid State Phys. 18 (1985) 3829, https://doi.org/10.1088/0022-3719/18/19/021.

[44] H.T. Ahmed, O.G. Abdullah, Impedance and ionic transport properties of proton-conducting electrolytes based on polyethylene oxide/methylcellulose blend polymers, J. Sci. Adv. Mater. Devices 5 (2020) 125–133, https://doi.org/10.1016/J.JSAMD.2020.02.001.

[45] A.K. Arof, S. Amirudin, S.Z. Yusof, I.M. Noor, A method based on impedance spectroscopy to determine transport properties of polymer electrolytes, Phys. Chem. Chem. Phys. 16 (2014) 1856–1867.

[46] N.M.A.C. Daud, N. Tamchek, I.M. Noor, Preparation and characterization of GG-LiCF3SO3-DMSO gel polymer electrolyte for potential lithium-ion battery application, J. Adv. Ther. Sci. Res. 9 (2022) 69–83, https://doi.org/10.15377/2409-5826.2022.09.6.

[47] V. Cyriac, S. Molakalu Padre, G.S.C. Ismayil, C. Chavan, R. Fakeerappa Bhajantri, M.S. Murari, Tuning the ionic conductivity of flexible polyvinyl alcohol/sodium bromide polymer electrolyte films by incorporating silver nanoparticles for energy storage device applications, J. Appl. Polym. Sci. 139 (2022) e52525, https://doi.org/10.1002/APP.52525.

[48] A. Abdukarimov, I.S.M. Noor, O. Mamatkarimov, A.K.M. Arof, Influence of charge carrier density, mobility and diffusivity on conductivity–temperature dependence in polyethylene oxide–based gel polymer electrolytes, High Perform. Polym. 34 (2022) 232–241, https://doi.org/10.1177/09540083211052841/ASSET/IMAGES/LARGE/10.1177_09540083211052841-FIG2.JPEG.

[49] N. Srivastava, M. Kumar, Ion dynamics and relaxation behavior of NaPF6-doped polymer electrolyte systems, J. Solid State Electrochem. 20 (2016) 1421–1428, https://doi.org/10.1007/S10008-016-3147-1/FIGURES/9.

[50] A.M. Abo El Ata, S.M. Attia, T.M. Meaz, AC conductivity and dielectric behavior of CoAlxFe 2-xO4, Solid State Sci. 6 (2004) 61–69, https://doi.org/10.1016/j.solidstatesciences.2003.10.006.

[51] K. Funke, B. Roling, M. Lange, Dynamics of mobile ions in crystals, glasses and melts, Solid State Ion. 105 (1998) 195–208, https://doi.org/10.1016/S0167-2738(97)00465-7.

[52] M.A. Brza, S.B. Aziz, N.M. Sadiq, Dielectric properties and ion transport studies from Trukhan, EIS, and Bandara-Mellander approaches for plasticized sodium ion conducting polymer blend electrolytes, Ionics 29 (2023) 1847–1861, https://doi.org/10.1007/S11581-023-04933-Z/FIGURES/6 (Kiel).

[53] N.K. Karan, O.K. Pradhan, R. Thomas, B. Natesan, R.S. Katiyar, Solid polymer electrolytes based on polyethylene oxide and lithium trifluoro- methane sulfonate (PEO–LiCF3SO3): ionic conductivity and dielectric relaxation, Solid State Ion. 179 (2008) 689–696, https://doi.org/10.1016/J.SSI.2008.04.034.

[54] V. Cyriac, I.M.N. Ismayil, K. Mishra, C. Chavan, R.F. Bhajantri, S.P. Masti, Ionic conductivity enhancement of PVA: carboxymethyl cellulose poly-blend electrolyte films through the doping of NaI salt, Cellulose 29 (2022) 3271–3291, https://doi.org/10.1007/s10570-022-04483-z.
[55] F. Colò, F. Bella, J.R. Nair, M. Destro, C. Gerbaldi, Cellulose-based novel hybrid polymer electrolytes for green and efficient Na-ion batteries, Electrochim. Acta 174 (2015) 185–190, https://doi.org/10.1016/j.electacta.2015.05.178.
[56] T. Pongjanyakul, A. Priprem, S. Puttipipatkhachorn, Investigation of novel alginate−magnesium aluminum silicate microcomposite films for modified-release tablets, J. Control. Release 107 (2005) 343–356, https://doi.org/10.1016/J.JCONREL.2005.07.003.
[57] J.P. Soares, J.E. Santos, G.O. Chierice, E.T.G. Cavalheiro, Thermal behavior of alginic acid and its sodium salt, Eclética Química 29 (2004) 57–64, https://doi.org/10.1590/S0100-46702004000200009.
[58] S. Tellamekala, P. Ojha, G. N.O, H. Nagabhushana, R. Ch, Effect of K+ ion doping on structural and physical properties of PVA/MAA:EA polymer blend electrolytes, Mater. Res. Innov. (2020) 1–13, https://doi.org/10.1080/14328917.2020.1795336.
[59] N.S. Rani, J. Sannappa, T. Demappa, Mahadevaiah, Effects of CdCl2 concentration on the structural, thermal and ionic conductivity properties of HPMC polymer electrolyte films, Ionics 21 (1) (2014) 133–140, https://doi.org/10.1007/S11581-014-1151-Y (Kiel)21 (2014).
[60] M.S. Su'ait, A. Ahmad, H. Hamzah, M.Y.A. Rahman, Effect of lithium salt concentrations on blended 49% poly(methyl methacrylate) grafted natural rubber and poly(methyl methacrylate) based solid polymer electrolyte, Electrochim. Acta 57 (2011) 123–131, https://doi.org/10.1016/J.ELECTACTA.2011.06.015.
[61] K. Wang, S. Ju, Q. Gao, G. Xia, G. Wang, H. Yan, L. Dong, Z. Yang, X. Yu, Porous sulfurized poly(acrylonitrile) nanofiber as a long-life and high-capacity cathode for lithium–sulfur batteries, J. Alloys Compd. 860 (2021), 158445, https://doi.org/10.1016/J.JALLCOM.2020.158445.
[62] M.H. Khanmirzaei, S. Ramesh, Studies on biodegradable polymer electrolyte rice starch (RS) complexed with lithium iodide, Ionics 20 (5) (2013) 691–695, https://doi.org/10.1007/S11581-013-1031-X (Kiel)20 (2013).
[63] S.K.S. Basha, M.C. Rao, Spectroscopic and electrochemical properties of PVP based polymer electrolyte films, Polym. Bull. 75 (8) (2017) 3641–3666, https://doi.org/10.1007/S00289-017-2229-2, 75 (2017).
[64] S.K.S. Basha, G.S. Sundari, K.V. Kumar, M.C. Rao, Preparation and dielectric properties of PVP-based polymer electrolyte films for solid-state battery application, Polym. Bull. 75 (3) (2017) 925–945, https://doi.org/10.1007/S00289-017-2072-5, 75 (2017).
[65] W. Kong, Y. Lei, Y. Yuan, C. Zhou, J. Lei, Preparation and investigation of solid polymer electrolyte based on novel polyamide elastomer/metal salt, Macromol. Res. 25 (8) (2017) 864–870, https://doi.org/10.1007/S13233-017-5094-9, 25 (2017).
[66] J.Y. Hwang, S.T. Myung, Y.K. Sun, Sodium-ion batteries: present and future, Chem. Soc. Rev. 46 (2017) 3529–3614, https://doi.org/10.1039/c6cs00776g.
[67] N. Krishna Jyothi, K. Vijaya Kumar, G. Sunita Sundari, P. Narayana Murthy, Ionic conductivity and battery characteristic studies of a new PAN-based Na+ ion conducting gel polymer electrolyte system, Indian J. Phys. 90 (2016) 289–296, https://doi.org/10.1007/s12648-015-0758-9.
[68] S.B. Aziz, I. Brevik, M.H. Hamsan, M.A. Brza, M.M. Nofal, A.M. Abdullah, S. Rostam, S. Al-Zangana, S.K. Muzakir, M.F.Z.Z. Kadir, Compatible solid polymer electrolyte based on methyl cellulose for energy storage application: structural, electrical, and electrochemical properties, Polymers 12 (2020) 2257, https://doi.org/10.3390/POLYM12102257 (Basel)Page12 (2020) 2257.
[69] J. Liu, Z. Bao, Y. Cui, E.J. Dufek, J.B. Goodenough, P. Khalifah, Q. Li, B.Y. Liaw, P. Liu, A. Manthiram, Y.S. Meng, V.R. Subramanian, M.F. Toney, V. V. Viswanathan, M.S. Whittingham, J. Xiao, W. Xu, J. Yang, X.Q. Yang, J.G. Zhang, Pathways for practical high-energy long-cycling lithium metal batteries, Nat. Energy 4 (3) (2019) 180–186, https://doi.org/10.1038/s41560-019-0338-x, 4 (2019).
[70] R. Cao, K. Mishra, X. Li, J. Qian, M.H. Engelhard, M.E. Bowden, K.S. Han, K. T. Mueller, W.A. Henderson, J.G. Zhang, Enabling room temperature sodium metal batteries, Nano Energy 30 (2016) 825–830, https://doi.org/10.1016/J.NANOEN.2016.09.013.
[71] M. Raja, A.M. Stephan, Natural, biodegradable and flexible egg shell membranes as separators for lithium-ion batteries, RSC Adv. 4 (2014) 58546–58552, https://doi.org/10.1039/c4ra08491h.
[72] Y. Zhu, F. Wang, L. Liu, S. Xiao, Z. Chang, Y. Wu, Composite of a nonwoven fabric with poly(vinylidene fluoride) as a gel membrane of high safety for lithium ion battery, Energy Environ. Sci. 6 (2013) 618–624, https://doi.org/10.1039/C2EE23564A.
[73] Y. Zhu, Y. Yang, L. Fu, Y. Wu, A porous gel-type composite membrane reinforced by nonwoven: promising polymer electrolyte with high performance for sodium ion batteries, Electrochim. Acta 224 (2017) 405–411, https://doi.org/10.1016/J.ELECTACTA.2016.12.030.
[74] J. Zhang, H. Wen, L. Yue, J. Chai, J. Ma, P. Hu, G. Ding, Q. Wang, Z. Liu, G. Cui, L. Chen, *In situ* formation of polysulfonamide supported poly(ethylene glycol) divinyl ether based polymer electrolyte toward monolithic sodium ion batteries, Small 13 (2017), 1601530, https://doi.org/10.1002/SMLL.201601530.
[75] G. Rajesha Shetty, B. Lakshmeesha Rao, Preparation and characterization of silk fibroin-polyvinyl alcohol (PVA) blend films for food packaging materials, Mater Today Proc. (2022), https://doi.org/10.1016/J.MATPR.2022.02.034.
[76] Pradeep Nayak, Ismayil, Vipin Cyriac, Shreedatta Hegde, Ganesh Sanjeev, M. S. Murari, Y.N. Sudhakar, Magnesium ion conducting free-standing biopolymer blend electrolyte films for electrochemical device application, J. Non-Cryst. Solids 592 (2022) 121741, https://doi.org/10.1016/j.jnoncrysol.2022.121741.